1   **Reactive transport modeling of leaking CO$_2$-saturated brine along a fractured pathway**

2

3   Nawaz Ahmad[a,b,*], Anders Wörman[a], Andrea Bottacin-Busolin[c], and Xavier Sanchez-Vila[d]

4   [a] Department of Civil and Architectural Engineering, KTH Royal Institute of Technology,

5   Brinellvägen 23, 10044, Stockholm, Sweden

6   [b] Policy Wing, Ministry of Petroleum and Natural Resources, Islamabad, Pakistan

7   [c] School of Mechanical, Aerospace and Civil Engineering, University of Manchester, United

8   Kingdom

9   [d] Hydrogeology Group, Department of Geotechnical Engineering and Geosciences,

10   Universitat Politècnica de Catalunya, UPC-BarcelonaTech, 08034 Barcelona, Spain

11

12   *Corresponding author: Nawaz Ahmad, Department of Civil and Architectural Engineering,

13   KTH Royal Institute of Technology, Brinellvägen 23, 10044, Stockholm, Sweden.

14   Email: nawaza@kth.se

15   Tel: +46 8 7909261

16

17

18   ABSTRACT

19   One concern regarding the underground storage of carbon dioxide (CO_2) is its potential

20   leakage from reservoirs. Over short period of time, the leakage risk is related mainly to

21   CO_2 as a separate supercritical fluid phase. However, over longer periods upon

22   complete dissolution of injected CO_2 in the fluid, the leakage risk is associated with

23   dissolved phase CO_2. Over the geological time scales, large-scale groundwater motion

24   may cause displacement of brine containing dissolved CO_2 along the conducting

25   pathways. In this paper, we present a comprehensive modeling framework that describes the

26   reactive transport of CO_2-saturated brine along a fracture in the clay caprock based on the

27   future, hypothetical leakage of the dissolved phase CO_2. This study shows that the transport

28   of leaked dissolved CO_2 is significantly retarded by a combination of various physical and

29   geochemical processes, such as mass exchange between conducting fracture and the

30   neighboring rock matrix through molecular diffusion, sorption and calcite dissolution in the

31   rock matrix. Mass stored in aqueous and adsorbed states in the rock matrix caused retention of

32   dissolved CO_2 along the leakage pathway. Calcite dissolution reaction in the rock matrix

33   resulted in consumption of leaking dissolved CO_2 and reduced its mass along the leakage

34   pathway. Consumption and retention of dissolved CO_2 along the leakage pathway have

35   important implications for analyzing the potential reduction of CO_2 fluxes from storage

36   reservoirs over large periods and long travel pathways.

37

38

39   **Keywords:** CO_2-saturated brine leakage, Reactive transport, Fracture, Matrix diffusion,

40   Sorption, Calcite kinetic reaction

Contents

89

90

1.   Introduction

The CO_2 geological sequestration has been proposed for mitigating the imbalance of gas emissions (Holloway, 1997, 2005; IPCC, 2002; Middleton et al., 2012). CO_2 is injected in deep subsurface geological reservoirs in a dense supercritical state (IPCC, 2005). Due to its lower density compared to the resident brine, the injected CO_2 tends to accumulate towards the top of the reservoir (Arts et al., 2005; Audigane et al., 2005; Pruess, 2006(a); Orr, 2009). Over short periods (up to 100 years), CO_2 is stored as a separate fluid phase (CO_{2g}) in the reservoir (physical trapping) (Audigane et al., 2005). However, CO_{2g} dissolves in the formation brine at the brine-CO_{2g} interface (solubility and ionic trapping) (Orr, 2009; IPCC, 2005). The resulting CO_2–saturated brine becomes slightly denser with respect to its original value, which causes gravity-driven downward flow, produces fingering, enhances fluids mixing, and increases CO_{2g} dissolution (Audigane et al., 2007). It might take almost 10,000 years for complete dissolution of injected CO_{2g} into the formation fluid (Audigane et al., 2005, 2007). Dissolution of CO_{2g} in the formation fluid lowers the pH of the resulting brine, driving heterogeneous geochemical reactions that result in fixation of CO_2 through precipitation of carbonate minerals (Audigane et al., 2005; Gunter et al., 1993). This process, termed mineral trapping, dominates over thousands to millions of years (Gunter et al., 1993; IPCC, 2005).

One concern related to the underground storage of CO_{2g} is its potential to leak from the storage reservoir (Haugan & Joos, 2004; Pruess, 2005; Stone et al., 2009). As long as injected CO_{2g} stays as a separate fluid phase in the reservoir (tens of years), higher leakage risk exists due to its lower density as compared to the resident fluid (Pruess, 2006a, 2006b). At large times, upon complete dissolution of CO_{2g} in the formation fluid, leakage risk is associated to the presence of CO_2 in dissolved phase (Bachu et al., 1994). Audigane et al., 2007 found that all the injected CO_{2g} was completely dissolved in the formation fluid after 10,000

116   years whereas only 5% was consumed through mineral reactions. Thus, after thousands

117   of years, only CO_2-saturated brine in the reservoir is expected, and the risk for

118   leakages of CO_2 is associated only with its dissolved phase (CO_{2aq}).

119   Large-scale groundwater motion may cause bulk displacement of brine out of the

120   reservoir with associated CO_{2aq} leakage risk (Bachu et al., 1994; IPCC, 2005; Gaus,

121   2010). In the sedimentary basins, groundwater flow velocities can be expected on the order of

122   millimeters to centimeters per year (Bachu et al., 1994). Thus due to low groundwater

123   velocities the leakage risk of CO_{2aq} is substantially lower than that of CO_{2g}. Transport of

124   CO_{2aq} may take place by advection, dispersion and diffusion processes (Bachu et al., 1994).

125   Although fractures act as the principal conductors for flow, the neighboring rock matrix also

126   plays a significant role in the solute transport processes (Grisak & Pickens, 1980). The

127   reactive species that diffuse from the fractures into the matrix may undergo sorption on the

128   surface of the solid and may react with the minerals in the rock matrix, which would

129   significantly inhibit the transport of reactive or non-reactive species in fractured rocks (Bodin

130   et al., 2003; Cvetkovic et al., 1999; Neretnieks, 1980; Xu et al., 2001). Thus, the interplay

131   between the conducting fracture and the matrix through diffusion is important for

132   understanding the transport of leaking CO_2-saturated brine.

133   Particularly, along the transport pathway, CO_{2aq} may undergo physical and geochemical

134   interactions with the existing rock formation minerals. These CO_2-rock interactions can

135   enhance transport by increasing hydraulic conductivity, linked to the porosity increases

136   caused by mineral dissolution, or decrease transport by decreasing the permeability due to

137   mineral precipitation. For example, a carbonate mineral filling the fracture could dissolve and

138   widen the existing flow path (Gaus, 2010). Calcite dissolution and precipitation along the

139   leakage pathway may result in a net conversion and uptake of CO_{2aq}. Kaufmann &

140   Dreybrodt, 2007 have reported the conversion of CO_{2aq} due to calcite dissolution in a ternary

141 $CaCO_3$-H_2O-CO_2 system. This indicates the relevance of studying the physical and

142 geochemical interactions of leaking CO_2-saturated brine in rock formations along the flow

143 pathway.

144 To date, no studies have been published in which retention and consumption of CO_{2aq} is

145 analyzed based on a physico-geochemical formulation of coupling transport in fractures,

146 molecular diffusion in the porous rock matrix (matrix diffusion) and reactions on available

147 rock surfaces in the matrix. So far, only few experimental and relatively simple numerical

148 modeling studies have been published related to the leakage of dissolved CO_2 (Gaus, 2010).

149 Gherardi et al., 2007 performed numerical simulations of the geochemical interactions of

150 caprock with leakage of the CO_2 gas phase and the associated brine simultaneously. These

151 authors found that calcite dissolution or precipitation was the most significant process that

152 controlled the chemical evolution of the caprock and responsible for changes in the porosity

153 near the reservoir-caprock interface. Ellis et al., 2011 conducted a seven-day experiment to

154 investigate the evolution of a fractured carbonate caprock due to geochemical interactions

155 with leaking CO_2-acidified brine. Andreani et al., 2008 reported experimental studies

156 regarding the fracture evolution due to cyclic flows of CO_2 dissolved in brine and the free-

157 phase CO_2. These authors reported an increase in porosity of 50% near the fracture, mainly

158 due to calcite dissolution. Nogues et al., 2013 analyzed the evolution of medium porosity and

159 pore-scale permeability caused by inflowing CO_2-saturated water. These authors concluded

160 that the geochemical modeling could be simplified by not including the reactions of minerals

161 kaolinite, anorthite, and albite whenever carbonate minerals are abundant. Peters et al., 2014

162 reported that a complex set of factors and processes are involved in permeability variations

163 resulting from dissolution of calcite in the caprock flow pathways caused by acidified brine

164 containing CO_{2aq}. These authors recommend including the complex geochemical interactions

7

165 of CO_2-saturated brine with calcite into reactive transport models to properly predict the flow

166 paths' permeability evolution.

167 The aim of the present study is to provide a quantitative understanding of the transport of

168 CO_2-saturated brine along fractured pathways, leaking from deep storage reservoir caused by

169 large-scale groundwater flow over geological time scales. This study analyzes the retention

170 and consumption of CO_{2aq} due to various physical and geochemical processes in the rock

171 matrix adjacent to the main flow conducting pathway. In this study we present a

172 comprehensive reactive transport model capable of analyzing the evolution of porosity along

173 the leakage pathway due to dissolution and precipitation of calcite over the period of time.

174 The novel approach adopted here explicitly couples the relatively fast transport of CO_{2aq} in

175 the fracture with slow transport in the neighboring rock matrix through molecular diffusion,

176 while accounting for various physical and geochemical processes, such as sorption, various

177 aqueous phase equilibria, and calcite mineral kinetic reactions in the rock matrix.

178 The full system of equations describing the reactive transport in terms of the chemical

179 components is presented here in a comprehensive form that can be efficiently solved using

180 numerical methods. The model framework is applied to a scenario that is believed to represent

181 the leakage of CO_{2aq} in a brine solution that is slowly flowing through a fracture in a clayey

182 caprock caused by regional-scale groundwater motion. Various transport scenarios are

183 performed over a period of 500 years to evaluate the significance of various physical and

184 geochemical processes on the mobility and consumption of CO_{2aq} in geochemical reactions

185 along the leakage pathway. Sensitivity analysis is then performed to analyze the effects of

186 various parameters (i.e. advective velocity in the fracture, sorption partition coefficient,

187 pressure and temperature conditions, and diffusion coefficient) on the retention and

188 consumption of CO_{2aq} along the leakage pathway. Comparative analysis between various

189 reactive transport scenarios is presented in terms of variations in medium porosity, retention

190 of CO_{2aq} caused by mass stored in aqueous and adsorbed states, mass uptake of CO_{2aq} in

191 geochemical reactions, and transport retardation along the leakage pathway.

192

193 **2.   Mathematical and numerical model**

194 *2.1.   Numerical solution technique*

195 The batch and the reactive transport modeling are performed in COMSOL Multiphysics that

196 is based on the finite element method. Fast aqueous phase reactions are modeled as

197 equilibrium reactions governed by the law of mass action. In contrast, the kinetics of calcite

198 mineral are considered slow and modeled as kinetically controlled. Aqueous phase reactions

199 are considered in both the fracture and the surrounding rock matrix whereas mineral

200 kinetic reactions are considered only in the rock matrix. In this study the concentration

201 of chloride (Cl^-) is taken equal to a constant value of 0.5 mol/(kg water) by considering

202 it as a conservative solute that does not participate in any of the geochemical reactions.

203

204 In this study the transport problem and the geochemistry are solved in a partially

205 coupled mode. Transport of aqueous species in the conducting fracture is modeled

206 through the advection-dispersion-reaction transport equation, whereas diffusion and

207 reaction are considered as the transport processes in the rock matrix. While considering a

208 constant velocity in the fracture, the transport processes in the fracture are modeled

209 independently of variations in porosity and permeability taking place in the rock

210 matrix. Aqueous phase equilibrium reactions are considered in conducting fracture and

211 neighbouring rock matrix, however calcite dissolution and precipitation is only

212 considered in the rock matrix. This simplification seems reasonable for a constant fluid

213 velocity taken in the fracture. Diffusion in the rock matrix is characterized by an effective

214 diffusivity, being a function of porosity of the rock matrix, and thus varying in time

215   and space caused by geochemical reactions. Further the mineral kinetic reactions in the

216   rock matrix are modeled as a function of medium porosity and mineral reactive surface

217   area that also vary in time and space. Spatial and temporal variations in minerals'

218   reactive surface area, medium porosity and permeability in the rock matrix are updated

219   based on the minerals dissolution/precipitation.

220   The mass conservation of aqueous species is formulated in terms of chemical

221   component species (u) that are linear combination of aqueous species (c) (Yeh &

222   Tripathi, 1991; Steefel & Lasaga, 1994). The methodology is presented by Saaltink et

223   al., 1998 (Appendix A). The consumption or production of chemical components in the

224   transport equation appears through the reaction term that represents the combined

225   effect of aqueous phase equilibrium and mineral kinetic reactions. In this study, the

226   equilibrium state obtained from the numerical solution of the background batch

227   geochemical modeling is used as initial conditions in the subsequent transport

228   modeling. This way, the solution of transport system requires only specifying the

229   boundary conditions in terms of chemical components.

230

231   Time-marching is performed by using an implicit nonlinear solver based on the

232   backward differentiation formula (BDF) with the Jacobian matrix updated at each

233   iteration. The variables are solved using a segregated solver technique that splits the

234   solution process into sub-steps, each one having individual numerical settings. In the

235   segregated technique the iteration process is continued until convergence. All the

236   solution sub-steps used the damped version of Newton's method with all damping

237   factors set equal to unity. The transport equation and the system of algebraic equations

238   required for speciation are solved together in segregated step-1. The ordinary

239 differential equation (ODE) required for mass conservation of kinetically controlled

240 minerals is solved in segregated step-2.

241 *2.2. Geochemical system for brine-rock interactions*

242 The set of geochemical reactions that describe the brine-rock chemical interactions is

243 presented in Table 1. Five of the reactions ((R0) through (R4)) represent aqueous phase

244 equilibrium reactions whereas the last reaction (R5) represents the kinetic reaction of

245 mineral calcite. The reaction (R0) that represents the equilibrium between CO_{2g} and

246 CO_{2aq} is only considered in the batch geochemical modeling. This reaction is excluded

247 in the subsequent reactive transport modeling due to the fact that CO_{2g} is not modeled.

248 In this study, the solubility model of Duan & Sun, 2003 (modified by Duan et al., 2006) is

249 used to model the dissolution of injected CO_{2g} in the saline water (0.5 M NaCl). This

250 solubility model is valid for a wide range of temperatures, pressures and ionic

251 strengths, that also takes into account the effects of dissolved species Na^+, Cl^-, K^+,

252 Ca^{2+}, Mg^{2+}, and SO_4^{2-}. The equilibrium constants for the reactions ((R1) through (R5))

253 are calculated as a function of temperature and are based on the default thermodynamic

254 database of "The Geochemist's Workbench (GWB)".

255

256 **Table 1.** Chemical reactions considered for $CaCO_3$-H_2O-CO_2 system.

No.	Reactions and equilibrium reaction constants
(R0)[1]	$CO_{2g} \leftrightarrow CO_{2aq}$
(R1)[2]	$H_2O + CO_{2aq} \leftrightarrow H^+ + HCO_3^-$
(R2)[2]	$H_2O \leftrightarrow H^+ + OH^-$
(R3)[2]	$HCO_3^- \leftrightarrow H^+ + CO_3^{2-}$
(R4)[2]	$Na^+ + HCO_3^- \leftrightarrow NaHCO_{3aq}$
(R5)[2]	$CaCO_3 + H^+ \leftrightarrow Ca^{2+} + HCO_3^-$

257 1. Equilibrium reaction constant is based on Duan & Sun, 2003 as modified by Duan et al.,

258 2006; 2. Equilibrium reaction constants are taken from The Geochemist's Workbench (GWB)

259 (default thermodynamic data for the GWB).

11

260 *2.3.   Batch geochemical modeling (BGM)*

261 *2.3.1. Background BGM*

262 Before performing the reactive transport modeling the equilibrated geochemical conditions in

263 the transport domain are obtained from the background BGM. Background BGM is also

264 performed for the reservoir to know the geochemical conditions under natural conditions prior

265 to dissolution modeling of injected CO_{2g}. The background BGM is performed for water-rock

266 interactions at a temperature of 45°C and a CO_2 partial pressure (P_{CO_2}) of 0.01 bar until

267 equilibrium with respect to mineral calcite is reached. During subsequent reactive transport

268 modeling, the equilibrated water chemistry obtained from the background BGM in the

269 transport domain ensures that the reactivity can be attributed solely to the concentrations of

270 the dissolved species in the CO_2-saturated brine leaking from the deep storage reservoir.

271 *2.3.2. CO_{2g} dissolution reaction modeling in the reservoir*

272 The water chemistry resulting from the background BGM is used as an initial condition for

273 CO_{2g} dissolution reaction modeling. The CO_{2g} dissolution reaction modeling is performed at

274 a temperature of 45°C and at a pressure of 105 bar (Gherardi et al., 2007). These values are

275 representative of the conditions expected at top boundary of the reservoir at a depth of 1040 m

276 below the land surface for assumed pressure and temperature gradient of 0.1 bar/m and 0.03

277 °C/m below the land surface (Pruess, 2008). In CO_{2g} dissolution reaction modeling, partial

278 pressure of CO_{2g} is increased to 105 bar from its background pressure of 0.01 bar. The

279 resulting water chemistry from the CO_{2g} dissolution reaction modeling is used as a boundary

280 condition for the subsequent reactive transport modeling.

281 *2.4.   Reactive transport*

282 *2.4.1. Conceptual transport model*

283 The conceptual transport model presented in Figure 1 shows the CO_2 storage reservoir

284 (bottom) and the clayey caprock (top). Only the fracture-matrix system in the clayey caprock

285   overlying the deep geological reservoir is included in the transport simulations. Assuming no

286   material fill-ins, porosity of the conducting fracture is taken as unity. In the coupled

287   fracture-matrix system, W_f is the half-fracture spacing, W_m is the matrix width and L is the

288   length of the fracture and the matrix. Symmetry is assumed at the left boundary (center of the

289   fracture) and right boundary of the rock matrix. The sizes of the modeled transport domain are

290   arbitrarily taken as $L=$ 20 m, $W_f=$ 1 mm, and $W_m=$ 10 m. For the base-case transport

291   scenarios, a constant fluid vertical velocity of 3.171×10^{-7} m/s (10 m/year) is used in the

292   fracture, whereas velocity is assumed to be zero in the rock matrix. This velocity magnitude in

293   the fracture is considered representative of Darcy's velocities on the order of 1 to 10 cm/year

294   for large-scale groundwater motion in bedrock continuum formed by the deep sedimentary

295   basins reported by Bachu et al., 1994. The considered length (20 m) of the transport pathway

296   is believed to be relevant for the considered flow velocity in the fracture and for a simulation

297   time of 500 years. The initial porosity of the rock matrix (clayey caprock) of 12% is selected

298   from the mineralogical composition reported in Table 2.
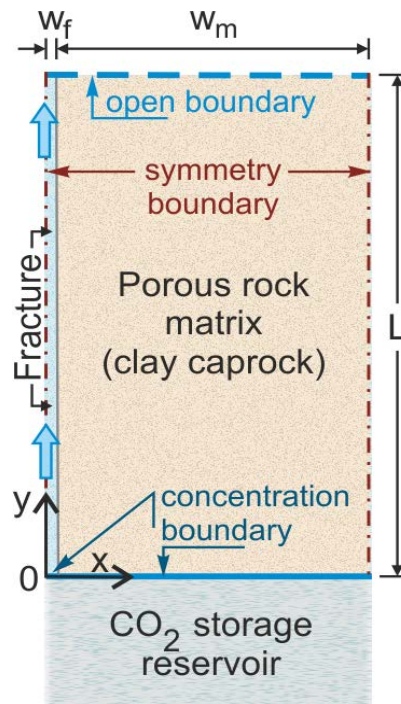
299

300   **Figure 1**. Schematic of the transport domain (clayey caprock containing a vertical fracture)
301   lying above the CO_2 geological storage reservoir.

302

303 **Table 2.** Clay caprock mineralogical composition (Gherardi et al., 2007).

Minerals	Volume fraction in solid rock	Volume fraction in porous rock (12% porosity)
Calcite	0.29	0.255
Dolomite	0.04	0.035
Quartz	0.20	0.176
Illite	0.02	0.018
K-feldspar	0	0
Chlorite	0.06	0.053
Albite	0	0
Kaolinite	0.05	0.044
Na-smectite	0.15	0.132
Muscovite	0.19	0.1672

304

305 *2.4.2. Reactive transport system for mobile species*

306 Reactive flow and transport modeling is performed for a single-phase CO_2-saturated brine

307 that also contains other species. The solute transport in the fracture-matrix system can be

308 conceptualized as a dual-domain system, where the transport along the fracture is driven by

309 advection, dispersion and diffusion whereas, in the matrix, transport only occurs by diffusion

310 (Steefel & Lichtner, 1998a, 1998b; Novak, 1993, 1996). The following reactive transport

311 equation, for multiple dissolved species (mobile ones) in a single aqueous phase and time

312 dependent porosity, is used (COMSOL):

313 $$\mathbf{R_f}\theta\frac{\partial \mathbf{c}}{\partial t} + \left(1 - \mathbf{K_d}\rho_p\right)\mathbf{c}\frac{\partial \theta}{\partial t} - \nabla \cdot [(\mathbf{D_D} + \mathbf{D_e})\nabla\mathbf{c}] + \nabla \cdot (\mathbf{vc}) = \theta\mathbf{r_{kin}} \quad (1)$$

314 In the above equation $\nabla = (\partial/\partial x, \partial/\partial y)$ is Nabla operator; $\theta(x,y,t)$ is the porosity (updated in

315 space and time) of the rock matrix; $\mathbf{c}(x,y,t)$ is a vector of the concentration [mol/(kg water)]

316 of all aqueous species; $\rho_p(x,y,t)$ is the particle density [kg/m^3] of the rock formation; $\mathbf{D_D}$

317 is the dispersion tensor [m^2/s]; $\mathbf{D_e} = \theta\mathbf{D_b}$ is the effective diffusion (diagonal) tensor

318 [m^2/s] defined as a function of medium porosity with $\mathbf{D_b}$ is a tensor of diffusion

319 coefficients of the involved species; $\mathbf{v}(x,y,t)$ is the Darcy's velocity vector [m/s] (pore

320 velocity times porosity); $\mathbf{r_{kin}}(x,y,t)$ is the sink/source [mol/(s kg water)] term in vector form

14

321   that represents consumption/production of species due to all of the geochemical reactions

322   (aqueous phase equilibrium as well as calcite kinetics) and $\mathbf{R_f}(x,y,t)$ is a diagonal matrix of

323   retardation factors due to sorption of mobile species on the surface of immobile mineral

324   phases.

325

326   The order of this reactive transport system can be reduced by expressing the species

327   concentration vector ($\mathbf{c}$) in term of chemical components concentration vector ($\mathbf{u}$). The

328   procedure for expressing the species concentration in terms of the chemical components for

329   reducing the order of the reactive transport system is presented in Appendix A. Following this

330   procedure, we present the reactive transport equation (1) in terms of the chemical components

331   concentration ($\mathbf{u}$) as follows:

332 $$\mathbf{R_f}\theta \frac{\partial \mathbf{u}}{\partial t} + \left(1 - \mathbf{K_d}\rho_p\right)\mathbf{u}\frac{\partial \theta}{\partial t} - \nabla \cdot [(\mathbf{D_D} + \mathbf{D_e})\nabla \mathbf{u}] + \nabla \cdot (\mathbf{vu}) = \theta \mathbf{r_{kin}} \quad (2)$$

333   where the retardation factor due to sorption of mobile species on the surface of immobile

334   rock matrix is defined by the following relation (COMSOL):

335 $$\mathbf{R_f} = 1 + \frac{\rho_{bulk}}{\theta}\mathbf{K_d} \quad (3)$$

336   In equation (3), $\rho_{bulk} = (1 - \theta)\rho_p$ is the bulk density [kg/(m^3 bulk volume)] of the

337   porous rock matrix defined as a function of porosity of the medium and $\mathbf{K_d}(x,y,t)$

338   represents a diagonal matrix whose diagonal elements are the sorption partition

339   coefficients [m^3/kg] of the involved component species. Using the component form, the

340   reactive transport system defined by equations (2) and (3) now involves only four components

341   rather than the eight species involved in the original system (Appendix A). Therefore vector

342     $\mathbf{u}$ in equation (2) has 4 components whereas $\mathbf{R_f}$ and $\mathbf{K_d}$ are 4×4 matrices. The transport

343   equation (2) is a nonlinear partial differential equation in which all the variables (θ, θ_p,

344   θ_{bulk}, $\mathbf{D_e}$, the matrices $\mathbf{K_d}$ and $\mathbf{R_f}$ as well as the vector $\mathbf{r_{kin}}$) are nonlinear function of

345   the local concentration of component species ($\mathbf{u}$) and are thus updated in time and

346 space. The reaction term ($\mathbf{r_{kin}}$) represents the consumption or production of component

347 species due to the combined effects of all geochemical reactions.

348 *2.4.3. Mass conservation of mineral phases (immobile species)*

349 The mass conservation of minerals (considered as immobile) undergoing kinetic reactions is

350 modeled using the following ODE:

351
$$\frac{\partial \mathbf{c_{m,bulk}}}{\partial t} = -\theta \rho_b \mathbf{r_m} \qquad (4)$$

352 where $\mathbf{c_{m,bulk}}$(x,y,t) is a vector of mass of all kinetically controlled minerals expressed

353 as mol/(m^3 bulk volume) which is calcite alone in this study; ρ_b is the fluid density

354 taken equal to 1000 kg/m^3; $\mathbf{r_m}$ (x,y,t) is a vector representing the consumption or

355 production [mol/(s kg water)] of the mineral phases due to their kinetically controlled

356 reaction (equation 5). The initial values of mineral mass ($c_{m,bulk}$) are calculated from

357 their initial volume fractions in the porous rock matrix.

358 *2.4.4. Minerals kinetic reaction (dissolution/precipitation)*

359 Slow mineral reactions are characterized by the kinetic reaction rate (r_m), which is defined as

360 the rate of conversion of the reactants into products per unit time and kg of water. The

361 kinetically controlled reaction of minerals is defined as a function of mineral reaction rate

362 constant, the concentration of aqueous species involved and the mineral reactive surface area

363 as follows (Lasaga et al., 1994):

364
$$r_m = k_m A_m \left[1 - \frac{Q_m}{K_m} \right] \qquad (5)$$

365 where k_m is the temperature-dependent kinetic rate constant [mol/(s m^2)], A_m is the specific

366 reactive surface area of the mineral [m^2/(kg water)], Q_m is the ion activity product of the

367 mineral and K_m is the equilibrium constant for the mineral-water interaction. The

16

368   temperature dependency of the mineral kinetic rate constant is described by the

369   Arrhenius equation (Lasaga, 1984):

370
$$k_m = k_{25} exp\left[-\frac{E_a}{R}\left(\frac{1}{T} - \frac{1}{298.15}\right)\right] \qquad (6)$$

371   where R is the gas constant, equal to 8.314 J/(mol K), T is absolute temperature [K],

372   E_a is the activation energy [J/mol] of the mineral and k_{25} is the rate constant [mol/(s

373   m^2)] of mineral at 25°C. The parameters and initial value of variables used in equations

374   (4) through (6) for mineral calcite are presented in Table 3.

375   **Table 3**. Parameters and initial values of variables used in equations (4)-(6) for mineral
376   calcite.

k_{25}* [mol/(s m^2)]	E_a* [KJ/mol]	A_m** [m^2/(kg water)]	$c_{m,bulk}$** [mol/(m^3 bulk volume)]
1.60×10-9	41.87	38.68	6912.5

377   * From Svensson & Dreybrodt, 1992; **Initial values are calculated from initial
378   volume fraction (corresponding to initial caprock porosity of 0.12) of minerals in
379   porous rock matrix. The minerals reactive surface area is taken equal to 10% of the
380   calculated physical surface area of the respective minerals.
381

382   *2.4.5. Activity coefficients of aqueous species*

383   The participation of aqueous species in the geochemical reactions is considered in the form of

384   their effective concentration or activity (a) rather than their concentration to account for non-

385   ideality of the aqueous solution (Langmuir, 1997; Betheke, 2008). The activity (dimensionless

386   quantity) of aqueous species is related to their concentration (c_i) and the activity coefficient

387   (γ_i) by the following relation (Lide et al., 2010):

388
$$a_i = \gamma_i \frac{c_i}{c_0} \qquad (7)$$

389   where c_0 is the standard concentration [1 mol/(kg water)]. The species activity coefficient is

390   found as a function of species concentrations in the solution. The model presented by Duan &

391   Sun, 2003 is used to calculate the activity coefficient of CO_{2aq}. The activity coefficients of

392   electrically charged species are calculated using the extended Debye-Hückel function (B-dot

393   equation). The B-dot equation is valid for NaCl dominant solutions up to ionic strength of 3

394   molal and for temperature conditions ranging from 0°C to 300°C (Betheke, 2008). The

395   activity coefficients of electrically neutral species are calculated using the relations presented

396   by Betheke, 2008(Appendix B).

397   *2.4.6. Mineral reactive surface area*

398   Minerals kinetic reactions cause variations in the corresponding reactive surface areas (A_m).

399   In this study, the geometric approach is adopted for the calculation of minerals reactive

400   surface (Johnson et al., 2004; Marini, 2007). The variations in A_m are modeled using the

401   following relationship developed in this study:

402
$$A_m = 0.1 \left(\frac{A_g}{\theta \rho_b V_g} \right) \left(MV c_{m,bulk} \right) \qquad (8)$$

403   where A_g, V_g, represents the physical surface area and volume of a mineral grain respectively

404   assuming a spherical grain with a radius of 1.65×10^{-5} m; MV is the molar volume of mineral;

405     $c_{m,bulk}$ is the mass of mineral updated in space and time through equation (4). The factor 0.1

406   shows the fraction of the mineral's reactive surface area to its geometrical surface area

407   (Johnson et al., 2004). Equation (8) also accounts for the effects of fluid density.

408   *2.4.7. Medium porosity*

409   Minerals dissolution or precipitation change volume fractions (through equation 4)

410   which in turn cause spatial and temporal variations in porosity. These are modeled as a

411   function of variations in volume fractions of the minerals in the porous media:

412
$$\theta = 1 - VF_{rock,p} \qquad (9)$$

413   where $VF_{rock,p} = \sum_{m=1}^{n} VF_{m,p}$ is the sum of the volume fractions of all the minerals

414   composing the porous rock; $VF_{m,p} = V_{m,p}/V_{rock,p}$ [m^3/m^3] is the volume fraction of the

415   mineral, expressed as the ratio of the mineral volume to the total volume of the porous

416   media. Some numerical restrictions are applied (Xu et al., 2014): (1) none of the

417 minerals are allowed to completely dissolve and disappear from the transport domain

418 by setting a minimum threshold concentration value of 1×10^{-7} [mol/(m^3 bulk volume)];

419 (2) medium porosity is not allowed to fall below 1×10^{-3} by limiting further mineral

420 precipitation.

421 *2.4.8. Dispersion and diffusion of mobile species*

422 The longitudinal dispersion in the fracture is defined by the Taylor-Aris dispersion formula as

423 follows (e.g., Bodin et al., 2003):

424
$$D_D = D_L = \frac{2}{105}\mathbf{v}^2 W_f^2 \mathbf{D_b}^{-1} \qquad (12)$$

425 where $\mathbf{v}$ is the vertical fluid velocity in the fracture and $\mathbf{D_b}$ is the diagonal matrix of the

426 molecular diffusion coefficient of the component species. At a constant temperature, the

427 values of $\mathbf{D_b}$ are calculated from the diffusion coefficient of CO_{2aq} in water as follows (Al-

428 Rawajfeh, 2004; Hassanzadeh et al., 2008):

429
$$\mathbf{D_b} = 10^{-0.87\log\left(\frac{\mu_b}{\mu_0}\right)} D_0 \mathbf{I} \qquad (13)$$

430 where $\mathbf{I}$ is the identity tensor, and μ_0 and μ_b are the viscosities of water and brine,

431 respectively. The viscosity of the brine is calculated from the model presented by Mao &

432 Duan, 2009 (Appendix C). The diffusion coefficient of CO_{2aq} in pure water is calculated from

433 the following relationship (Hassanzadeh et al., 2008):

434
$$D_0 = 10^{-4.1764+\frac{712.52}{T}-\frac{2.591\times10^5}{T^2}} \qquad (14)$$

435 The calculated values of μ_0, μ_b, D_0, and D_b for a 0.5 M NaCl solution and at various

436 temperature and pressure values are presented in Table 4. The diffusion coefficients for all

437 component species are taken equal to the calculated value of the diffusion coefficient of

438 CO_{2aq} (Gherardi et al., 2007).

439

19

440　**Table 4.** Calculated values of viscosities and molecular diffusion coefficients at various
441　pressure and temperature conditions.

Pressure and Temperature	μ_0 [Pa s]	μ_b[Pa s]	D_0 [m^2/s]	D_b[m^2/s]
105 bar and 45°C	5.96×10^{-4}	6.27×10^{-4}	3.19×10^{-9}	3.05×10^{-9}
155 bar and 60°C	4.69×10^{-4}	4.94×10^{-4}	4.25×10^{-9}	4.05×10^{-9}

442

443　*2.4.9. Sorption of mobile species on the rock medium surfaces*

444　The diagonal matrix of sorption partition coefficients ($\mathbf{K_d}$) used in equation (3) can be defined

445　from the equilibrium sorption reaction (Bodin et al., 2003; Bear & Cheng, 2010):

446
$$[\mathbf{K_d}]_{i,i} = \frac{[c_i]_s}{[c_i]_{aq}}\bigg|_{eq} \qquad (15)$$

447　where $[c_i]_s$ is the species concentration adsorbed on the solid (immobile) phase, expressed as

448　the species concentration per unit mass of the solid [mol/kg] phase, and $[c_i]_{aq}$ is the

449　concentration of the solute (mobile) in the fluid phase [mol/m^3]. However in this study the

450　sorption process is modeled using a constant value of partition coefficient (K_d) taken equal to

451　2.5×10^{-4} m^3/kg for all the component species in the base-case transport scenarios.

452

453　Various minerals have shown to adsorb CO_{2aq} (Santschi & Rossi, 2006; Tabrizy et al., 2013).

454　Santschi & Rossi, 2006 found that the adsorption of CO_2 on calcite surfaces depends on the

455　adsorbed H_2O. Furthermore, these authors suggest that the adsorption of CO_2 on calcite

456　surfaces results from specific interaction with a bifunctional surface intermediate

457　$(Ca(OH)(HCO_3))$, which serves as a site for CO_2 adsorption. Their study shows that calcite

458　has specific adsorption sites that accommodate additional CO_2 quantities beyond their regular

459　aqueous dissolution process that were accounted for in this study. The partitioning coefficient

460　from the slope of Figure 2(b) presented in Santschi & Rossi, 2006 is deduced as 6.6×10^{-2}

461　m^3/kg. Fujii et al., 2010 conducted an experimental study of the sorption characteristics of

462　CO_2 on rocks and minerals at pressure and temperature conditions that were relevant for the

463　geological storage of CO_2. These authors observed the reversible nature of the CO_2 sorption

20

464   process. In their experimental studies, Heller & Zoback, 2014 reported the adsorption of CO_2

465   on various clay mineral samples under different pressure conditions. The authors found that

466   the clay type "Eagle Ford 127", which mainly consists of calcite (80%), had the lowest

467   capacity for CO_2 adsorption relative to the other clay samples. Table 5 presents the deduced

468   values of sorption partition coefficient for various clay samples from study of Heller &

469   Zoback, 2014 calculated from equation (6) and the values given in Table 2 of their study.

470
471   **Table 5**. Values of sorption partition coefficient K_d [m^3/kg] deduced from Heller & Zoback,
472   2014.

Clay sample	Barnett 31	Marcellus	Montney	Eagle Ford 127
Calcite content (%)	0	1	8.1	80
Clay content (%)	37.4	52	24.1	5
K_d [m^3/kg] value at 10.5 MPa	3.18×10^{-3}	1.54×10^{-3}	3.33×10^{-3}	7.39×10^{-4}
K_d [m^3/kg] value at 15.5 MPa	3.45×10^{-3}	1.62×10^{-3}	3.60×10^{-3}	7.93×10^{-4}

473

474   The values of sorption partition coefficient used in this study (7.50×10^{-4}, 2.50×10^{-4}, and

475   8.33×10^{-5} m^3/kg) are much lower than the values reported by Santschi & Rossi, 2006 and

476   Heller & Zoback, 2014. These authors used crushed rock, which has a higher reactive surface

477   area, rather than intact rock.

478   *2.4.10.   Initial and boundary conditions*

479   The initial and boundary conditions associated with the transport system formed by equations

480   (2) and (3) for the fracture and the rock matrix are presented as follows:

481   Initial conditions in the transport domain:

482    $\mathbf{u_i}(x, y, t) = \mathbf{u_{i,0}}$ (16)

483   Inflow (bottom of the fracture and the matrix):

484    $\mathbf{u_i}(y = 0, t) = \mathbf{u_{i,bc}}$ (17)

485   No flux (line of symmetry assumed at center of the fracture):

486    $-\mathbf{n} \cdot [(\mathbf{D_D} + \mathbf{D_e})\nabla\mathbf{u} + \mathbf{vu}] = 0$ for $x = 0$ (18)

487   No flux (line of symmetry assumed at right sided boundary of the rock matrix):

488    $-\mathbf{n} \cdot [(\mathbf{D_D} + \mathbf{D_e})\nabla\mathbf{u} + \mathbf{vu}] = 0$ for $x = W_f + W_m$ (19)

489   Outflow (top boundaries of the fracture and the rock matrix):

490    $-\mathbf{n} \cdot [(\mathbf{D_D} + \mathbf{D_e})\nabla\mathbf{u}] = 0$ for $y = L$ (20)

491   where $\mathbf{n}$ is a unit normal vector that is perpendicular to the boundary surface. This system is

492   completed by the continuity condition at the fracture-matrix interface boundary. The outflow

493   boundary condition assumes that the transport of species is only caused by advection. For a

494   zero fluid velocity in the rock matrix, the top of the rock matrix acts as a no flow boundary.

495   The inflow boundary conditions (constant fluid velocity in the fracture and constant species

496   concentration) are adopted as a basis for generic process analyses. A constant vertical velocity

497   is assumed to prevail in the fracture during the entire simulation time. The initial and

498   boundary conditions written in terms of component species are presented in Table 6.

499

500   **Table 6.** Initial (sub-index 0) and boundary conditions (sub-index bc).

Pressure and temperature	45°C and 105 bar	60°C and 155 bar
Component species	Concentration [mol/(kg water)]	Concentration [mol/(kg water)]
$u_{HCO_3,0}$	4.02×10^{-3}	3.10×10^{-3}
u_{Na_0}	5.00×10^{-1}	5.00×10^{-1}
u_{Ca_0}	2.01×10^{-3}	1.55×10^{-3}
$u_{CO_2,0}$	1.82×10^{-4}	1.38×10^{-4}
$u_{HCO_3,bc}$	7.17×10^{-2}	5.95×10^{-2}
$u_{Na_{bc}}$	5.00×10^{-1}	5.00×10^{-1}
$u_{Ca_{bc}}$	3.58×10^{-2}	2.97×10^{-2}
$u_{CO_2,bc}$	1.08	1.06

501

502 *2.4.11.   Various base-case transport scenarios*

503 Various base-case transport scenarios are analyzed for a period of 500 years (Table 7). Mass

504 transport without any geochemical reactions is analyzed in mass transport scenarios 1, 2 and 3

505 whereas the reactive transport is performed in reactive transport scenarios 4 and 5. These

506 base-case transport scenarios are performed for P and T values of 105 bar and 45°C

507 respectively. In these base-case transport scenarios, a constant fluid vertical velocity of

508 3.171×10^{-7} m/s (10 m/year) is used in the fracture.

509 **Table 7.** Various base-case transport scenarios.

Scenarios	Processes accounted for
1	No interaction between fracture and matrix
2	Molecular diffusion between fracture and matrix, no calcite mineral reaction in the matrix, no sorption in the matrix
3	Molecular diffusion between fracture and matrix, no calcite mineral reaction in the matrix, sorption in the matrix
4	Molecular diffusion between fracture and matrix, calcite mineral reaction in the matrix, no sorption in the matrix
5	Molecular diffusion between fracture and matrix, calcite mineral reaction in the matrix, sorption in the matrix

510

511 *2.4.12.   Sensitivity analysis*

512 Sensitivity analysis is performed to analyze the effects of different fluid vertical velocities (v)

513 in the fracture, the sorption partition coefficient (K_d), P and T values and the diffusion

514 coefficient on the mass uptake of CO_{2aq} in geochemical reactions. Two sets of P and T values

515 are considered; 105 bar and 45°C and 155 bar and 60°C, which are thought to represent

516 reservoir depths of 1040 m and 1540 m below the land surface respectively. For the

517 sensitivity analysis, the base-case transport scenarios 3 and 5 are further divided into sub-

518 scenarios for different velocities in the fracture, sorption partitioning coefficients, P and T

519 values and diffusion coefficient (Table 8). These scenarios 3 and 5 represent all the

520 considered transport processes (diffusion in the matrix, sorption on the rock surfaces in the

521 matrix and mineral kinetic reactions). Moreover, in the sensitivity analysis, the number of

522   mass transport scenarios (3.1, 3.2, 3.3, 3.4, 3a and 3b) equaled the number of reactive

523   transport scenarios (5.1, 5.2, 5.3, 5.4, 5a and 5b).

524   **Table 8.** Sensitivity analysis for various parameters using the base-case transport scenarios 3
525   and 5.

Sub-scenarios	Velocity in the fracture, v [m/s]	Distribution coefficient, K_d [m³/kg]	Pressure and temperature	Diffusion coefficient [m²/s]
3.1	3.17×10^{-8}	2.50×10^{-4}	105 bar and 45°C	3.05×10^{-9}
3.2	6.34×10^{-7}	2.50×10^{-4}	105 bar and 45°C	3.05×10^{-9}
3.3	3.17×10^{-7}	7.50×10^{-4}	105 bar and 45°C	3.05×10^{-9}
3.4	3.17×10^{-7}	8.33×10^{-5}	105 bar and 45°C	3.05×10^{-9}
5.1	3.17×10^{-8}	2.50×10^{-4}	105 bar and 45°C	3.05×10^{-9}
5.2	6.34×10^{-7}	2.50×10^{-4}	105 bar and 45°C	3.05×10^{-9}
5.3	3.17×10^{-7}	7.50×10^{-4}	105 bar and 45°C	3.05×10^{-9}
5.4	3.17×10^{-7}	8.33×10^{-5}	105 bar and 45°C	3.05×10^{-9}
3a	3.17×10^{-7}	2.50×10^{-4}	155 bar and 60°C	3.05×10^{-9}
5a	3.17×10^{-7}	2.50×10^{-4}	155 bar and 60°C	3.05×10^{-9}
3b	3.17×10^{-7}	2.50×10^{-4}	155 bar and 60°C	4.05×10^{-9}
5b	3.17×10^{-7}	2.50×10^{-4}	155 bar and 60°C	4.05×10^{-9}

526

527   *2.4.13. Calculation of mass uptake of CO_{2aq} in geochemical reactions*

528   The mass of CO_{2aq} consumed in the geochemical reactions in each reactive transport scenario

529   (scenarios 4, 5, 5.1, 5.2, 5.3, 5.4, 5a, and 5b) is calculated by comparing the CO_{2aq} mass

530   balances with the corresponding mass transport scenario (scenarios 2, 3, 3.1, 3.2, 3.3, 3.4, 3a

531   and 3b) for better accuracy. The mass uptake of CO_{2aq} in geochemical reactions is calculated

532   by mass balance considerations involving the cumulative mass entering and exiting through

533   the inflow and outflow boundaries, and that stored in the aqueous and adsorbed states within

534   the domain. In order to estimate the quantities of CO_{2aq} mass uptake in geochemical reactions

535   in relation to the mass inflow through the bottom inflow boundaries in each reactive transport

536   scenario, the mass uptake quantities are presented in terms of normalized mass uptake. The

537   normalized mass uptake of CO_{2aq} ($\boldsymbol{m_{con}^n = \frac{m_{con}}{m_{in}}}$) is the cumulative mass consumed ($\boldsymbol{m_{con}}$)

538   normalized with respect to the cumulative mass that entered the domain through the bottom

539   inflow boundaries ($\boldsymbol{m_{in}}$) over the period of time.

24

540
541 **3.   Results**

542 *3.1.   Background brine composition in the reservoir and the transport domain*

543 From the background BGM, the solution was found equilibrated at a pH of 7.26 and contains

544 Na^+ and Cl^- as the two major species representing the effects of brine, followed by HCO_3^-,

545 Ca^{2+}, $NaHCO_{3aq}$, and CO_{2aq} as the intermediate species that characterize the brine-rock

546 equilibrium with respect to calcite. The remaining species were present at trace levels (Table

547 9).

548 **Table 9.** Species concentrations from the background BGM at 45°C and 0.01 bar (column 2)
549 and from CO_{2g} dissolution reaction modeling performed at 45°C and 105 bar (column 3).

Pressure and temperature	45°C and 0.01 bar	45°C and 105 bar
Species	c [mol/(kg water)]	c [mol/(kg water)]
HCO_3^-	3.33×10^{-3}	6.04×10^{-2}
Na^+	4.99×10^{-1}	4.89×10^{-1}
Cl^-	5.00×10^{-1}	5.00×10^{-1}
Ca^{2+}	2.01×10^{-3}	3.58×10^{-2}
CO_{2aq}	1.98×10^{-4}	1.08
H^+	5.44×10^{-8}	1.67×10^{-5}
OH^-	1.29×10^{-6}	4.25×10^{-9}
CO_3^{2-}	1.43×10^{-5}	8.85×10^{-7}
$NaHCO_{3aq}$	6.63×10^{-4}	1.13×10^{-2}

550

551 *3.2.   Solubility of CO_{2g} and the resulting brine composition in the reservoir*

552 Due to the dissolution of CO_{2g}, the concentration of CO_{2aq} in the 0.5 M NaCl brine stabilized

553 at approximately 1.08 mol/(kg water), at a temperature of 45°C and pressure of 105 bar (see

554 Table 9). An increase in the concentration of CO_{2aq} resulted in a drop in pH from 7.26 to 4.78.

555 *3.3.   Reactive transport*

556 Initially, the dissolved species in the pore water in the transport domain of fracture-matrix

557 system were at chemical equilibrium and saturated with respect to the calcite mineral. The

558 mixing of leaking CO_2-saturated brine, also saturated with respect to calcite, with the parent

559 pore water in the transport domain disturbed the chemical equilibrium and turned the

560   geochemical conditions to undersaturation with respect to calcite in close vicinity of the

561   bottom inflow boundaries. This initiated the calcite reaction in the rock matrix. In the rock

562   matrix, calcite was allowed to dissolve or precipitate depending on the saturation state over

563   the period of time.

564   *3.3.1. Base-case transport scenarios*

565   Figure 2 shows the saturation state with respect to calcite at onset (1 second(s)) of the

566   simulation for scenario-4 (without sorption) and scenario-5 (with sorption) caused by mixing

567   of leaking CO_2-saturated brine with the resident water. The observed lower values of

568   saturation with respect to calcite were 0.09 and 0.04 in scenarios 4 and 5 respectively.
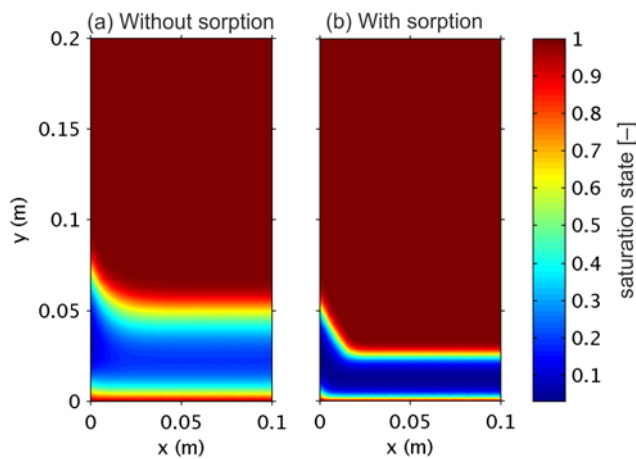
569
570   **Figure 2**. Saturation state of calcite at onset (1 s) of the simulation for (a); scenario-4 (without
571   sorption); and (b) scenario-5 (with sorption).
572

573   The decrease in saturation state with respect to calcite below unity initiated the calcite

574   dissolution reaction near the bottom (inflow) boundary in the rock matrix. Figure 3 shows the

575   calcite reaction rate for scenario-4 (no sorption) and scenario-5 (with sorption) at onset (1 s)

576   of the simulation. The difference in spread of reaction zones between Figures 3a and 3b is due

577   to the sorption that has constrained the transport of species in scenario-5. It can also be

578   observed that sorption causes relatively larger calcite kinetic reactions (either dissolution or

579   precipitation).

580
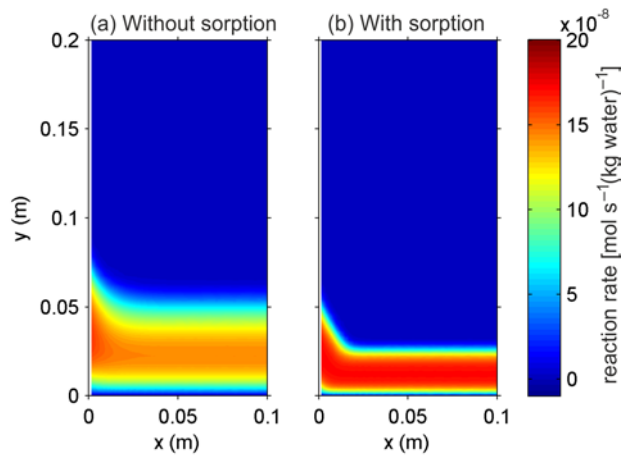
581

Figure 3. Calcite reaction rate [mol/(s kg water)] at onset (1 s) of the simulation for; (a) scenario-4 (without sorption); and (b) scenario-5 (with sorption).

The calcite dissolution reaction in the rock matrix driven by higher concentration of CO_{2aq} in the leaking brine caused the production of Ca^{2+} and HCO_3^- species (Kaufmann & Dreybrodt, 2007). The conversion of CO_{2aq} in the calcite dissolution reaction has spatially constrained the corresponding concentration plume relative to the other species (Ca^{2+} and HCO_3^-) due to their production in calcite dissolution reaction. Figure 4 shows the concentration plumes of CO_{2aq}, Ca^{2+} and HCO_3^- for scenario-5 (with sorption) after 500 years.
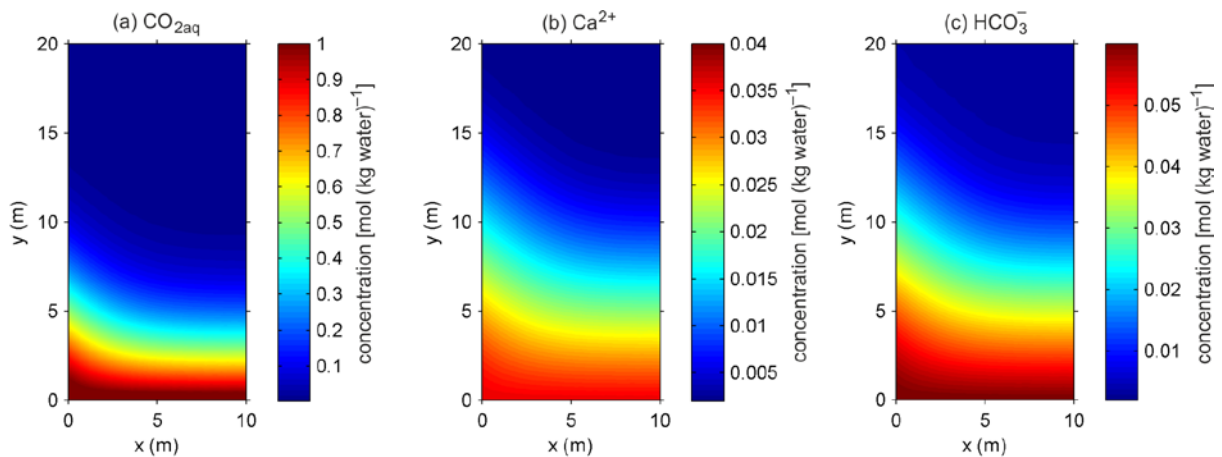

Figure 4. Spatial distribution of the concentrations [mol/(kg water)] of dissolved species after 500 years for scenario-5; (a) CO_{2aq}; (b) Ca^{2+}; and (c) HCO_3^{-1}.

597   Over time, calcite reaction in the rock matrix resulted in variations in the mass of calcite with

598   associated changes in the mineral reactive surface area. Figure 5a and 5b shows these

599   variations for scenario-5 after 500 years.

600
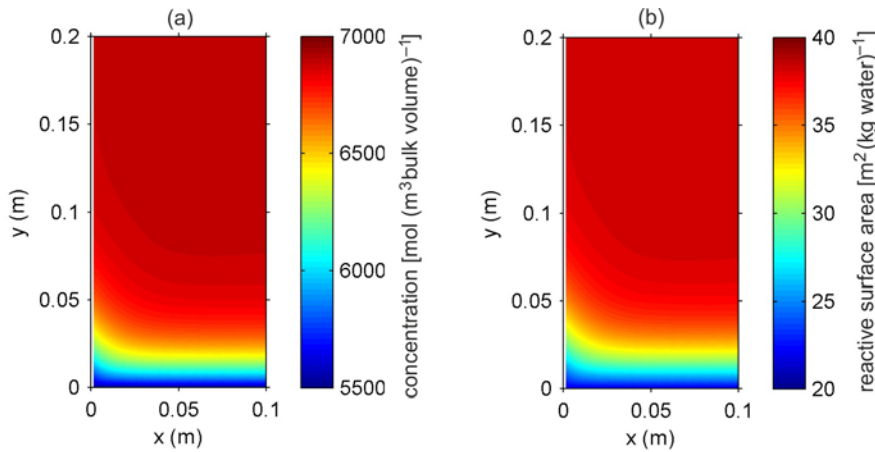
601
602
603   **Figure 5**. Effects of the calcite reaction on the; (a) mass of calcite [mol/(m^3 bulk volume)] for
604   scenario-5; (b) calcite reactive surface area [m^2/(kg water)] for scenario-5 after 500 years.
605

606   Variations in porosity (Figure 6a) and medium permeability (Figure 6b) as well as effective

607   diffusivity of dissolved species in the rock matrix (Figure 6c) for scenario-5 are also

608   presented. These variations have been observed mainly close to the bottom inflow boundary.
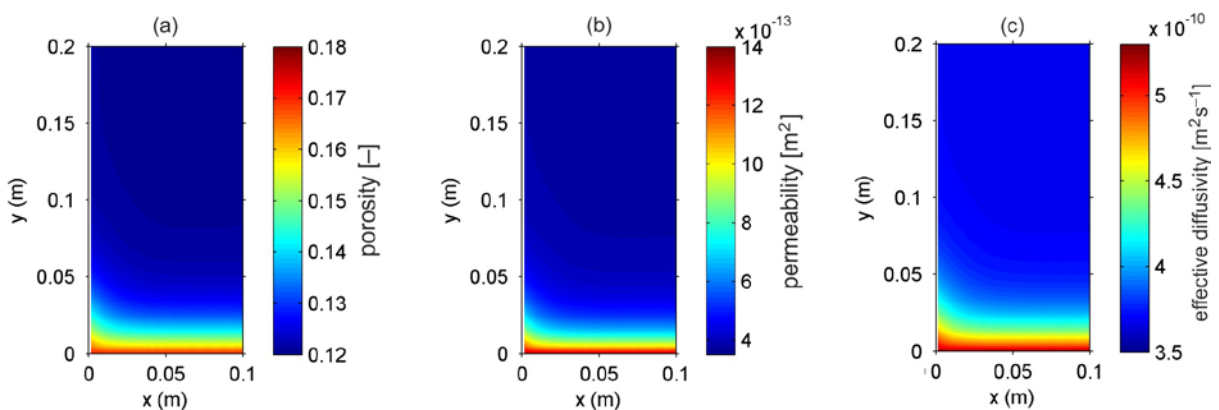
609

610   **Figure 6**. Effects of the calcite reaction on (a) medium porosity for scenario-5; (b) medium
611   permeability [m^2] for scenario-5; (c) effective diffusivity [m^2/s] for scenario-5 after 500 years.
612

613   Initially, the pore water in the fracture-matrix system had a pH of 7.26, while that in the CO_2-

614   injected reservoir was 4.78. Apart from mixing, pH was affected by both sorption and calcite

615   kinetic reaction in the rock matrix. Figure 7 shows how the pH in the fracture-matrix transport

616   domain evolves after 500 years for various transport scenarios. In the absence of calcite

617   reaction, the low pH spreads farther in scenario-2 (no sorption, Figure 7a) than in the

618   scenario-3 (with sorption, Figure 7b). The calcite kinetic reaction retards the transport of low

619   pH brine for scenario-4 (no sorption, Figure 7c) and scenario-5 (with sorption, Figure 7d).

620   The higher pH values observed in the reactive transport scenarios (4, 5) as compared to

621   mass transport scenarios (2, 3) are due to consumption of H^+ in the calcite dissolution

622   reaction.

623
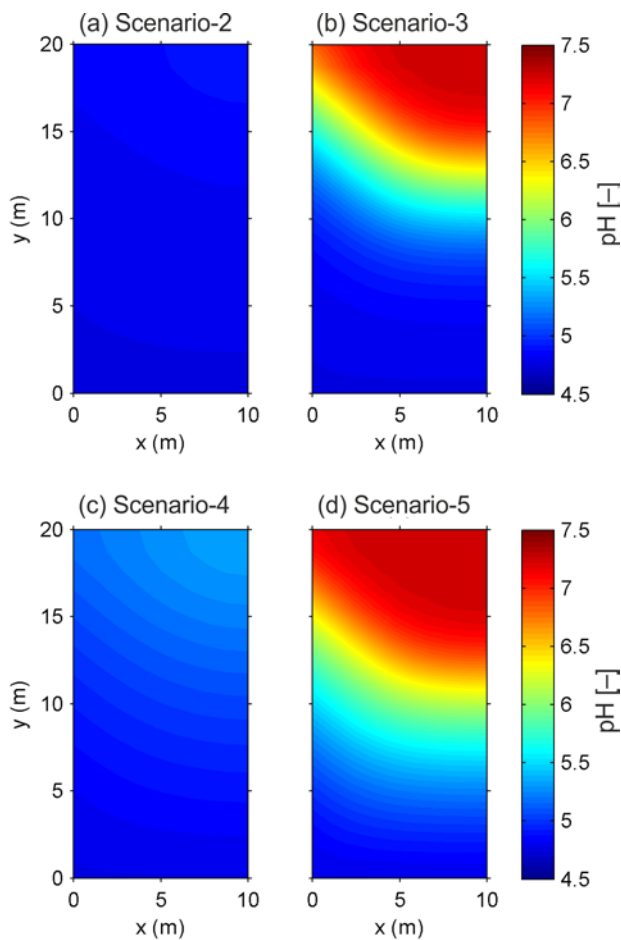
624
625 **Figure 7**. Evolution of pH in the fracture-matrix system after 500 years for various base-case
626 transport scenarios; (a) scenario-2 (no calcite reaction, no sorption); (b) scenario-3 (no calcite
627 reaction with sorption); (c) scenario-4 (calcite reaction, no sorption); and (d) scenario-5
628 (calcite reaction with sorption).

629

630   Figure 8 shows the normalized mass uptake of CO_{2aq} in percentage due to geochemical

631   reactions (aqueous phase equilibrium and calcite kinetic reactions) for the (i) no sorption and

632   (ii) sorption cases. After 500 years, the normalized mass uptake of CO_{2aq} declined to 4.43%

633   for the no sorption case whereas it was 4.97% when sorption was included in the analysis.

634   Although higher mass uptake of CO_{2aq} resulted in scenario-5 compared to scenario-4 (Table

635   10), the observed lower value of normalized mass uptake of CO_{2aq} in the former scenario

636   compared to the latter has been mainly due to the normalization of the mass uptake with

637   respect to the mass inflow through the bottom inflow boundaries in the respective scenario. At

638   the initial times of the simulation, sorption causes relatively higher concentration gradients

639   across the inflow boundaries in scenario-5 compared to those in scenario-4. Sorption process

640   fixes species' mass in adsorbed state on the rock surfaces and reduces species' mass in

641   aqueous state which in turn causes higher concentration gradients across the bottom inflow

642   boundaries.

643

644   Over the period of time, relatively lower saturation state with respect to calcite prevailed in

645   the rock matrix in scenario-5 compared to that in scenario-4. The sorption process caused a

646   relatively lower concentration of Ca^{2+} and HCO_3^{-1} in the aqueous state in scenario-5

647   compared to scenario-4 that resulted in lower saturation state of calcite in the former

648   scenario than the latter. The resulting lower saturation state of calcite caused relatively

649   higher calcite dissolution reaction thus contributing towards higher mass uptake of

650   CO_{2aq} in geochemical reactions in scenario-5 compared to that in scenario-4. Prevailing

651   higher mass uptake relative to mass inflow in scenario-5 resulted in higher normalized mass

652   uptake in scnario-5 compared to scenario-4 in the later times of the simulation. Lower mass

653   uptake relative to mass inflow in scenario-4 resulted in lower normalized mass uptake in this

654 scenario   than   that   in   scenario-5   after   nearly   277   years.
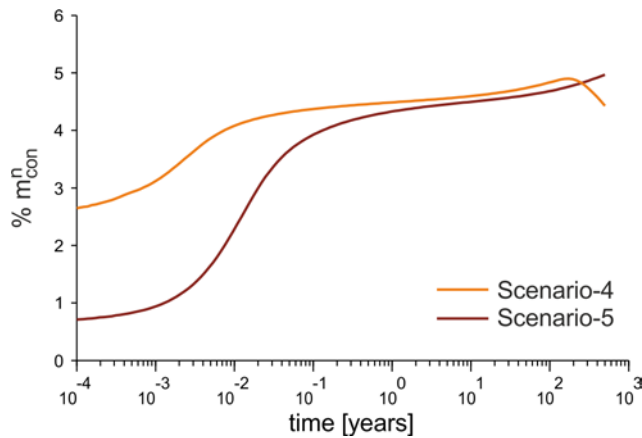
655

656

657 **Figure 8.** The percent normalized uptake of CO_{2aq} in geochemical reactions without sorption
658 (scenario-4) and with sorption (scenario-5).

659

660 Table 10 presents the mass balance of CO_{2aq} in the base-case reactive transport

661 scenarios 4 and 5 after 500 years of simulation time. A total of 6.26×10^2 [mol] and

662 1.45×10^3 [mol] of CO_{2aq} have been consumed in geochemical reactions over the period of

663 500 years in scenario-4 and scenario-5 respectively. Thus sorption in scenario-5 has caused

664 CO_{2aq} mass conversion (through geochemical reactions) approximately twice that observed

665 without sorption in scenario-4. This result is consistent with the increase in total pore volume

666 resulting from calcite dissolution in the rock matrix domain which was observed almost

667 double in scenario-5 compared to scenario-4 (see Table 12). For the same fluid velocity in the

668 fracture, higher total mass uptake of CO_{2aq} in scenario-5 compared to scenario-4 is (i)

669 mainly due to higher mass inflow through the bottom inflow boundaries in scenario-5

670 driven by sorption process, and (ii) to a lesser extent to relatively lower saturation state

671 of calcite caused by sorption in scenario-5 compared to scenario-4. Higher total mass

672 inflow in scenario-5 compared to that in scenario-4 resulted in overall higher calcite

673 dissolution and higher total mass uptake of CO_{2aq} in former scenario compared to the

31

674 latter. In Table 10 we can also observe that the mass of CO_{2aq} is conserved, with mass

675 balance errors lower than 0.10%.

676

677 **Table 10**. Mass [mol] balance of CO_{2aq} in the base-case reactive transport scenarios 4 and 5.

Scenarios	Scenario-4	Scenario-5
Total mass entered the domain	1.41×10^4	2.91×10^4
Mass entered the domain due to advection	5.39×10^3	5.39×10^3
Mass entered the domain due to diffusion	8.73×10^3	2.37×10^4
Mass entered the domain due to dispersion	9.15×10^{-5}	2.96×10^{-4}
Mass left the domain	4.27×10^2	9.63×10^{-1}
Mass stored in aqueous state	1.31×10^4	4.68×10^3
Mass stored in adsorbed state	0	2.30×10^4
Mass consumed in geochemical reactions	6.26×10^2	1.45×10^3
% normalized mass uptake of CO_{2aq} after 500 years	4.43	4.97
% error in mass balance	6.00×10^{-2}	7.33×10^{-2}

678

679 Due to the small width of the fracture (1 mm) compared to that of the rock matrix (10

680 m), and low advective velocity in the fracture, the total mass inflow (by advection,

681 dispersion and diffusion) through the bottom inflow boundary of the fracture is small

682 compared to that entering (by diffusion) through the bottom inflow boundary of the

683 rock matrix. Table 11 presents the division of total mass entered the domain through

684 the bottom inflow boundaries of fracture and matrix in reactive transport scenarios 4

685 and 5 for simulation time of 500 years.

686

687 **Table 11**. Mass [mol] of CO_{2aq} that entered the domain through bottom inflow boundaries of
688 fracture and rock matrix in the reactive transport scenarios 4 and 5.

Scenarios	Scenario-4		Scenario-5	
Bottom inflow boundary	fracture	matrix	fracture	matrix
Total mass entered the domain	5.39×10^3	8.73×10^3	5.39×10^3	2.37×10^4
Mass entered the domain due to advection	5.39×10^3	0	5.39×10^3	0
Mass entered the domain due to diffusion	4.46×10^{-1}	8.73×10^3	1.44×10^0	2.37×10^4
Mass entered the domain due to dispersion	9.15×10^{-5}	0	2.96×10^{-4}	0

689

32

690   Table 12 presents the mass balance of Ca^{2+} and calcite (mineral) for the reactive transport

691   scenarios 4 and 5 after 500 years. It can be observed that the mass [mol] of Ca^{2+} produced is

692   equal (except numerical errors of less than 0.5%) to the mass of calcite dissolved from the

693   kinetic reaction. Table 12 also presents the values of increase in total pore volume [m^3] due to

694   calcite dissolution in the rock matrix. An increase in the total pore volume of the rock matrix

695   is found due to higher calcite dissolution than its precipitation. It is found that in the reactive

696   transport scenarios 4 and 5 the pore volume reached values of 24.023 m^3 and 24.052 m^3

697   respectively from the initial value of 24 m^3.

698   **Table 12**. Mass [mol] balance of Ca^{2+}, mineral calcite and total pore volume of rock matrix in
699   the base-case reactive transport scenarios 4 and 5 after 500 years.

Scenarios	Scenario-4	Scenario-5
Mass [mol] of Ca^{2+} produced in dissolution of mineral calcite	6.22×10^2	1.41×10^3
Mass [mol] of mineral calcite dissolved	6.25×10^2	1.41×10^3
Increase in pore volume [m^3]	2.31×10^{-2}	5.21×10^{-2}
% error in mass balance	4.89×10^{-1}	2.35×10^{-1}

700

701   The retardation in transport of transported species along the fracture was analyzed in terms of

702   breakthrough curves representing the concentration of dissolved species at specified locations

703   along the fracture. Figure 9 presents the breakthrough curve of CO_{2aq} at the top (outflow)

704   boundary of the fracture for scenario-1, corresponding to no mass interaction between the

705   species in the fracture and those in the adjacent rock matrix. An observable increase in

706   concentration of CO_{2aq} at the outflow boundary of the fracture becomes visible only after 1.25

707   years. We observe that the concentration of CO_{2aq} at the outflow boundary has attained the

708   value equal to the one applied at the inflow boundary after only 2.8 years.

709
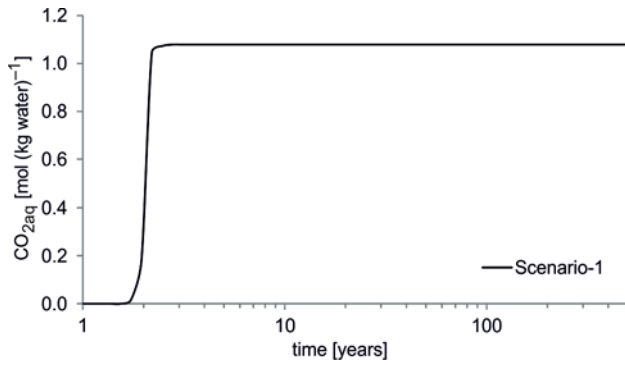
Figure 9. Breakthrough curve for the base-case transport scenario-1 showing the concentration of CO_{2aq} at top outflow of the fracture over the period of time.

Figure 10 presents the breakthrough curves for CO_{2aq}, for various base-case transport scenarios 2 through 5, at 10 m (mid-way of the fracture) and 20 m (top outflow boundary of the fracture). An observable increase in concentration of CO_{2aq} at 10 m and 20 m locations along the fracture becomes visible only after nearly 16 and 50 years, respectively. Comparing the breakthrough curves for scenario-1 (Figure 9) and scenario-2 (Figure 10a), it can be observed that the mass exchange between the conducting fracture and the adjacent rock matrix has caused significant retardation in the transport of CO_{2aq} in scenario-2. We can further see that sorption has also caused a significant retardation in the transport of CO_{2aq} (scenario-2 Vs scenario-3 and scenario-4 Vs scenario-5). Due to significant retardation caused by sorption, the concentration of CO_{2aq} does not increase, within the simulation period, to a level that would make it visible at top outflow boundary of the fracture in scenarios 3 and 5 (Figure 10b). Mass uptake of CO_{2aq} in geochemical reactions has also caused transport retardation. However, compared to sorption, the mass uptake of CO_{2aq} in geochemical reactions has caused relatively small retardation in its transport (scenario-2 Vs scenario-4 and scenario-3 Vs scenario-5).
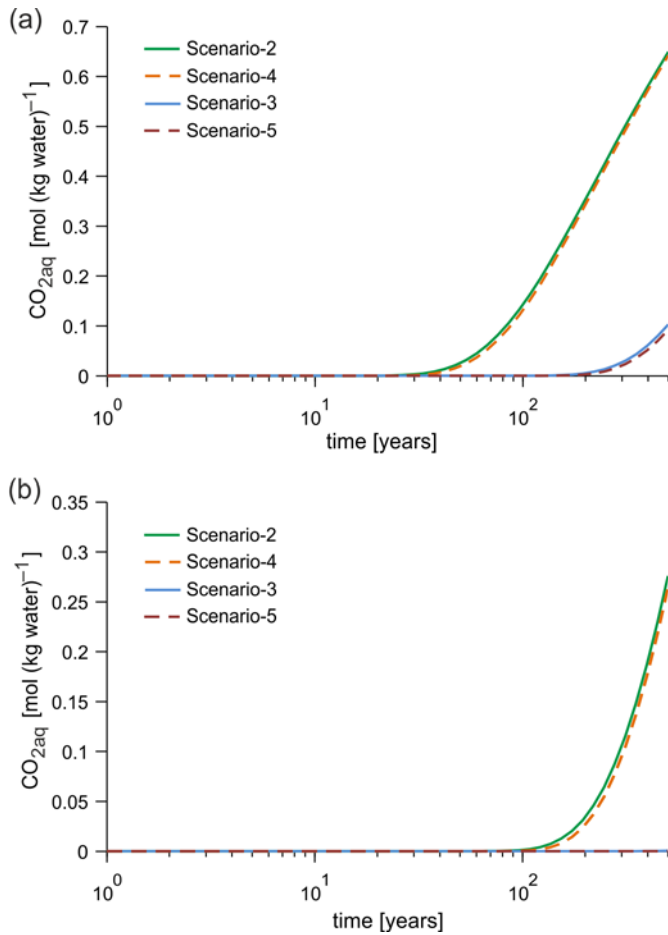
34

Figure 10. Breakthrough curves showing the concentration of CO_{2aq} for various base-case transport scenarios along the fracture, at; (a) 10 m from the inflow boundary; and (b) 20 m from the inflow boundary.

3.3.2. Sensitivity analysis

3.3.2.1. Role of fluid velocity in fracture and sorption partition coefficient

Figure 11 shows the normalized mass uptake of CO_{2aq} in geochemical reactions in the reactive transport scenarios (5.1, 5.2, 5.3, and 5.4) studied in the sensitivity analysis. For the same sorption partition coefficient, it can be observed in Figure 11(a) that the normalized mass uptake of CO_{2aq} decreased as the vertical velocity in the fracture increased (scenario-5.1 Vs scenario-5.2). On the other hand in Figure 11(b), for the same fluid velocity in the fracture, the normalized mass uptake decreased with increase in sorption partition coefficient (scenario-5.4 Vs scenario-5 and scenario-5.3).

35

745

746

747
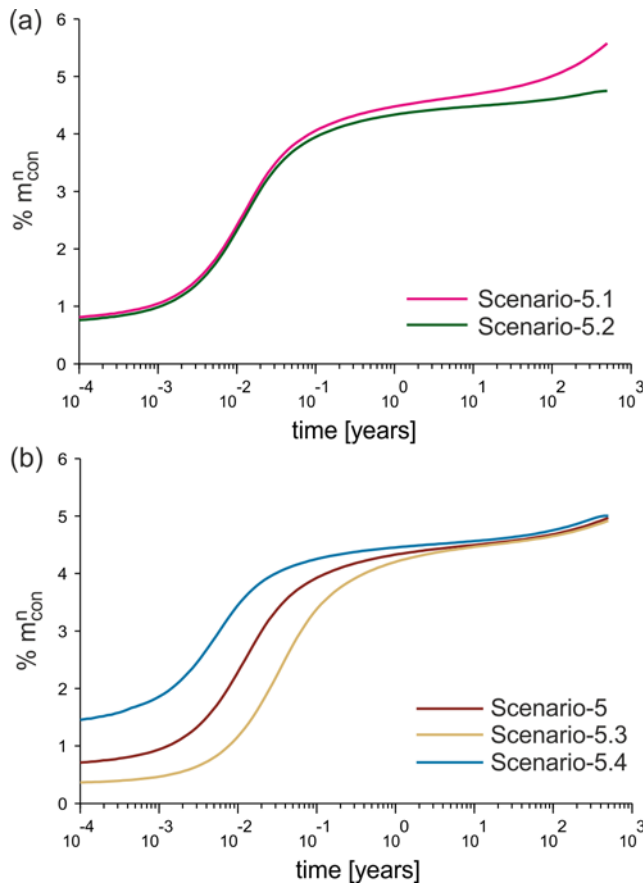
Figure 11. The percent normalized uptake of CO_{2aq} in geochemical reactions for various reactive transport scenarios; (a) scenarios 5.1 and 5.2; (b) scenarios 5, 5.3, and 5.4.

750

751   To elaborate the graphical results presented in Figure 11 we have also calculated the

752   overall mass balance of CO_{2aq} in the transport domain for the reactive transport

753   scenarios 5.1 through 5.4 (Table 13). In Table 13, higher mass uptake of CO_{2aq} can be

754   observed in scenario-5.2 (1.60×10^3 mol) compared to scenario-5.1 (1.41×10^3 mol),

755   however an opposite behaviour is observed in Figure 11(a). Higher fluid velocity in the

756   fracture in scenario-5.2 results in higher advective mass inflow through the bottom

757   inflow boundary of fracture. This caused a lower normalized CO_{2aq} mass uptake in

758   scenario-5.2 compared to that in scenario-5.1. Also from Table 10 and Table 13, higher

759   mass uptake of CO_{2aq} can be observed in scenario-5.3 (2.23×10^3 mol) compared to

36

760 scenario-5 ($1.45{\times}10^{3}$ mol) and scenario-5.4 ($1.03{\times}10^{3}$ mol) but the opposite behaviour

761 is observed in Figure 11(b). Lower sorption in scenario-5.4 causes lower diffusive

762 mass inflow mainly through the bottom inflow boundary of rock matrix which results

763 in higher normalized mass uptake in scenario-5.4 compared to scenarios 5 and 5.3.

764 Thus the normalized mass uptake trends presented in Figure 11, showing the opposite

765 of actual mass uptake (Table 13), are due to the normalization of the mass uptake with

766 respect to mass the inflow through the bottom inflow boundaries.

767 **Table 13**. Mass [mol] balance of CO_{2aq} in various reactive transport scenarios (5.1, 5.2, 5.3,
768 and 5.4) studied in the sensitivity analysis.

Scenarios	Scenario-5.1	Scenario-5.2	Scenario-5.3	Scenario-5.4
Total mass entered the domain	$2.59{\times}10^{4}$	$3.37{\times}10^{4}$	$4.53{\times}10^{4}$	$2.06{\times}10^{4}$
Mass entered the domain due to advection	$5.39{\times}10^{2}$	$1.08{\times}10^{4}$	$5.39{\times}10^{3}$	$5.39{\times}10^{3}$
Mass entered the domain due to diffusion	$2.53{\times}10^{4}$	$2.29{\times}10^{4}$	$3.99{\times}10^{4}$	$1.53{\times}10^{4}$
Mass entered the domain due to dispersion	$2.96{\times}10^{-5}$	$2.52{\times}10^{-4}$	$5.87{\times}10^{-4}$	$1.71{\times}10^{-4}$
Mass left the domain	$9.11{\times}10^{-2}$	$2.75{\times}10^{1}$	$9.11{\times}10^{-1}$	$1.85{\times}10^{1}$
Mass stored in aqueous state	$4.13{\times}10^{3}$	$5.42{\times}10^{3}$	$2.77{\times}10^{3}$	$7.41{\times}10^{3}$
Mass stored in adsorbed state	$2.03{\times}10^{4}$	$2.66{\times}10^{4}$	$4.03{\times}10^{4}$	$1.22{\times}10^{4}$
Mass converted in geochemical reactions	$1.41{\times}10^{3}$	$1.60{\times}10^{3}$	$2.23{\times}10^{3}$	$1.03{\times}10^{3}$
% normalized mass uptake of CO_2 after 500 years	5.46	4.75	4.91	5.00
% error in mass balance	$8.27{\times}10^{-2}$	$6.19{\times}10^{-2}$	$7.63{\times}10^{-2}$	$6.77{\times}10^{-2}$

769

770 Table 14 presents the mass balance of Ca^{2+} and calcite (mineral) for the reactive transport

771 scenarios 5.1 through 5.4 after 500 years. It also presents an increase in total pore volume

772 [m^{3}] which is well correlated with calcite dissolution in the rock matrix. It can also be

773 observed that the difference between the mass of calcite dissolved and Ca^{2+} produced is lower

774 than 0.36% in all these reactive transport scenarios.

Table 14. Mass [mol] balance of Ca^{2+}, mineral calcite and pore volume of rock matrix in various reactive transport scenarios (5.1, 5.2, 5.3, and 5.4) studied in the sensitivity analysis.

Scenarios	Scenario-5.1	Scenario-5.2	Scenario-5.3	Scenario-5.4
Mass [mol] of Ca^{2+} produced in dissolution of mineral calcite	1.37×10^3	1.56×10^3	2.13×10^3	1.01×10^3
Mass [mol] of mineral calcite dissolved	1.37×10^3	1.57×10^3	2.14×10^3	1.02×10^3
Increase in pore volume [m^3]	5.07×10^{-2}	5.79×10^{-2}	7.90×10^{-2}	3.75×10^{-2}
% error in mass balance	2.46×10^{-1}	2.11×10^{-1}	2.42×10^{-1}	3.02×10^{-1}

3.3.2.2. Role of temperature and diffusion coefficient

In addition to the base-case transport scenarios 3 and 5, which were performed at 105 bar and 45°C, transport scenarios 3a, 3b, 5a, and 5b were also performed at 155 bar and 60°C to analyze the effects of pressure and temperature and diffusion coefficient on the mass uptake of CO_{2aq} in geochemical reactions. Due to changes in P and T values, the initial and the boundary conditions required for transport modeling were also changed. These values were obtained by performing an additional background BGM and CO_{2g} dissolution modeling for these pressure and temperature conditions, and the results were presented in Table 6 (column 3). Results from CO_{2g} dissolution modeling showed that brine in the reservoir got saturated at relatively lower concentration of CO_{2aq} with increase in temperature (Table 6).

Table 15 presents the mass balance of CO_{2aq} in reactive transport scenarios 5a and 5b. For the same values of fluid velocity in the fracture, sorption partition coefficient and diffusion coefficient in scenarios 5 and 5a, relatively lower mass inflow in the latter scenario (2.85×10^4 mol) compared to that in the former one (2.91×10^4 mol) was due to lower concentration of CO_{2aq} in leaking CO_2-saturated brine as a result of higher temperature in scenarios 5a and 5b compared to rest of the scenarios. Lower mass uptake of CO_{2aq} in scenario-5a (1.29×10^3 mol) compared to that in scenario-5 (1.45×10^3 mol) is (i) mainly due to lower calcite

796 kinetic reaction with increased temperature in scenario-5a and (ii) to a lesser extent due

797 to lower mass inflow resulting from lower concentration of CO_{2aq} in the leaking brine

798 in scenario-5a.

799

800 For the same values of velocity in the fracture, sorption partition coefficient and

801 temperature in scenarios 5a and 5b, relatively higher mass inflow in the latter scenario

802 $(3.21 \times 10^4$ mol) compared to that in the former one (2.85×10^4) resulted from higher diffusion

803 coefficient used in scenario-5b than in scenario-5a. The higher mass inflow resulted in higher

804 total mass uptake in scenario-5b $(1.46 \times 10^3$ mol) compared to that in scenario-5a $(1.29 \times 10^3$

805 mol). Also the negligible error in mass balance shows that the condition of mass conservation

806 of CO_{2aq} is well satisfied by the numerical solution method.

807 Table 15. Mass [mol] balance of CO_{2aq} in reactive transport scenarios 5a, and 5b.

Scenarios	Scenario-5a	Scenario-5b
Total mass entered the domain	2.85×10^4	3.21×10^4
Mass entered the domain due to advection	5.29×10^3	5.29×10^3
Mass entered the domain due to diffusion	2.32×10^4	2.68×10^4
Mass entered the domain due to dispersion	2.85×10^{-4}	3.04×10^{-4}
Mass left the domain	7.44×10^{-1}	8.12×10^{-1}
Mass stored in aqueous state	4.60×10^3	5.18×10^3
Mass stored in adsorbed state	2.26×10^4	2.55×10^4
Mass converted in geochemical reactions	1.29×10^3	1.46×10^3
% normalized mass uptake of CO_2 after 500 years	4.529	4.534
% error in mass balance	7.36×10^{-2}	7.54×10^{-2}

808

809

810 Figure 12 presents the normalized mass uptake of CO_{2aq} in geochemical reactions in reactive

811 transport scenarios 5, 5a, and 5b. Higher temperature in scenarios 5a and 5b has resulted

812 in lower normalized mass uptake of CO_{2aq} in geochemical reactions in these scenarios

813 (4.53%) as compared to scenario-5 (4.98%) after 500 years. On the other hand due to same

814 temperature and thus the same calcite reaction kinetics, nearly the same normalized mass

815 uptake of CO_{2aq} resulted in scenarios 5a and 5b.

816
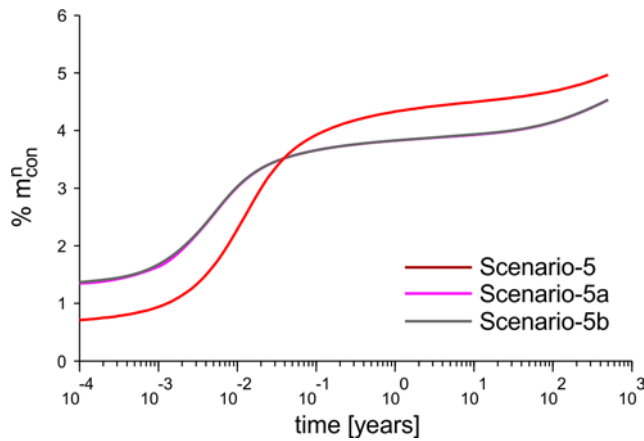
817

Figure 12. The percent normalized mass uptake of CO_{2aq} in geochemical reactions in reactive transport scenarios 5, 5a and 5b.

820

4.   Discussion

Dissolution of CO_{2g} in the reservoir brine made the solution more acidic by decreasing its pH from 7.26 to 4.78. The decrease in pH depends on the CO_{2aq} concentration in the solution and on the type of minerals in contact with the solution. In the analyzed geochemical system, mineral calcite provided a buffer and maintained the pH at a value of 4.78, which is slightly greater than the pH that would be expected in the absence of mineral calcite (Hellevang, 2006; Pokrovsky et al., 2009).

According to the stoichiometry of the calcite reaction (R5), H^+ is consumed from the solution and Ca^{2+} and HCO_3^- are produced. The reaction of H^+ with calcite is associated with the conversion of CO_{2aq} to H^+ (Dreybrodt et al., 1996; Kaufmann & Dreybrodt, 2007). The dissolution of calcite results in the conversion of CO_{2aq} from the solution, whereas the precipitation of calcite may result in the release of CO_{2aq} in the solution (Dreybrodt et al., 1997). Over time, calcite has either dissolved or precipitated depending on the geochemical conditions in the transport domain. However, the observed higher dissolution of calcite relative to its precipitation in the rock matrix has resulted in the net uptake of CO_{2aq}.

40

836   The calcite dissolution reaction, which was initiated near the bottom inflow boundary in the

837   rock matrix, resulted in the conversion of CO_{2aq} and the production of Ca^{2+} and HCO_3^-. This

838   simultaneous consumption and production associated with the transport of these species

839   brought the geochemical conditions towards calcite saturation in the transport domain over

840   the period of time. These saturated conditions resulted in calcite precipitation, as

841   demonstrated by the negative calcite reaction rates. However, the calcite reaction rates and the

842   reaction propagation in the matrix were found to be different between the no sorption case and

843   the sorption case. Over the period of time, the calcite kinetic reaction in the rock matrix

844   affected the transport of the CO_{2aq}, Ca^{2+} and HCO_3^- species. After 500 years the spread of

845   CO_{2aq} concentration plume (Figure 4a) was smaller than the concentration plumes of Ca^{2+} and

846   HCO_3^- (Figure 4b and 4c). This difference resulted from the conversion of CO_{2aq} with the

847   simultaneous production of Ca^{2+} and HCO_3^- in the calcite dissolution reaction.

848   The observed steep variations of normalized mass uptake of CO_{2aq} in geochemical

849   reactions at early times of the simulations in Figures 8, 11 and 12 are due to higher

850   calcite dissolution reaction with associated higher mass uptake of CO_{2aq} relative to the

851   mass inflow through the bottom inlet boundaries. At early times, the lowest saturation

852   state of calcite is caused by leaking CO_2-saturated brine on its entering the transport

853   domain. This results in higher calcite dissolution reaction with associated higher mass

854   uptake of CO_{2aq} relative to the mass inflow. However, over the period of time the

855   saturation state of calcite starts increasing due to production of Ca^{2+} and HCO_3^{-1},

856   which in turn results in decreasing calcite dissolution reaction with associated lower

857   mass uptake of CO_{2aq}. Also, over time the mass inflow of CO_{2aq} through the bottom

858   inflow boundaries keeps decreasing mainly due to decreasing diffusive fluxes. Thus,

859   after the initial times, almost steady state conditions are reached (mass uptakes of

860   CO_{2aq} Vs its mass inflows) in all the reactive transport scenarios with the exception of

861   scenario-4 where we observe declining trends of normalized mass uptake at later

862   simulation times.

863

864   The retardation in the transport of CO_{2aq} has been observed when one or more physical or

865   geochemical processes are considered (Figure 9, Figure 10a and Figure 10b). Among these

866   physical and geochemical processes, the aqueous phase mass storage of CO_{2aq} in pore spaces

867   of the rock matrix has played an important role in the inhibition of the transport of leaked

868   CO_{2aq}, followed by its sorption in the rock matrix and (to a lesser extent) by the mass uptake

869   of CO_{2aq} in geochemical reactions. The retention of CO_{2aq} due to sorption along the leakage

870   pathway was seen highly dependent on the magnitude of the sorption partitioning coefficient.

871   Thus, properly accounting for sorption is important for evaluating the fate of CO_{2aq} that leaks

872   from the storage reservoir along the leaky pathways.

873   In Figure 12, the observed variation in the normalized mass uptake of CO_{2aq} in

874   geochemical reactions between the reactive transport scenarios 5, 5a, and 5a was

875   mainly due to different calcite kinetics prevailing in these reactive transport scenarios.

876   Higher temperature in scenarios 5a and 5b resulted in (i) higher calcite kinetic rate

877   constant (9.44×10^{-9} [mol/(s m^2)]) in scenarios 5a and 5b than that in scenario-5 (4.63×10^{-9}

878   [mol/(s m^2)]), and (ii) lower calcite reaction equilibrium constant in scenarios 5a and 5b

879   (16.34) than in scenario-5 (26.76). At very early times, higher kinetic rate constant

880   causes higher calcite dissolution reaction rate in scenarios 5a and 5b compared to that

881   prevailing in scenario-5. At very early times of simulation, higher calcite dissolution

882   reaction rate causes higher mass uptake of CO_{2aq} and thus higher normalized mass

883   uptake in scenarios 5a and 5b compared to that in scenario-5.

884

885   As a result of lower equilibrium constant in scenarios 5a and 5b due to higher

886   temperature, the saturation state with respect to calcite was reached at relatively lower

887   values of reaction products (Ca^{2+} and HCO_3^-) and at higher value of reactants (H^+) than

888   those in scenario-5.. Also over the period of time, lower equilibrium constant in

889   scenarios 5a and 5b caused saturation state of calcite to increase more rapidly to a

890   relatively higher value in scenarios 5a and 5b compared to that in scenario-5. The

891   resulting higher saturation state of calcite in scenarios 5a and 5b caused a relatively

892   sharp decrease in calcite dissolution reaction in these scenarios than in scenario-5. As a

893   consequence after only 4.47×10^{-2} years (1.41×10^6 s), the calcite dissolution reaction

894   rate became higher in scenario-5 than that in scenarios 5a and 5b. This resulted in

895   higher normalized uptake of CO_{2aq} in geochemical reactions in scenario-5 compared to

896   that in scenarios 5a and 5b after 4.47×10^{-2} years. Thus in the very early times of

897   simulation, higher calcite kinetic rate constant causes higher mass uptake whereas after

898   4.47×10^{-2} years higher saturation state of calcite plays an important role and results in

899   lower mass uptake in scenarios 5a and 5b compared to that in scenario-5.

900   **5.   Conclusions**

901   In this study, we presented a reactive transport model to study the leakage of CO_2-saturated

902   brine through a fractured clay caprock. This model considers the relatively fast transport of

903   CO_2-saturated brine in the fracture (by advection, dispersion and diffusion), slow transport in

904   the rock matrix (by diffusion), sorption of CO_{2aq}, and various geochemical reactions including

905   calcite dissolution and precipitation in the rock matrix. The reactive transport problem was

906   solved in terms of chemical components. The presented numerical model showed accurate

907   mass balance of various aqueous species as well as kinetically controlled mineral calcite

908   involved in the reactive transport.

909 The mobility and spreading of CO_{2aq} along the leakage pathway was found to be controlled

910 by the following factors: the velocity magnitude of the brine in the conducting fracture, the

911 mass exchange between the fracture and the neighboring rock matrix through molecular

912 diffusion, the sorption and the kinetics of calcite mineral in the rock matrix. The kinetics of

913 the calcite reaction resulted in spatial and temporal variations in mass of calcite mineral, the

914 mineral reactive surface area, porosity of the medium, and the effective diffusivity of mobile

915 species in the rock matrix. Calcite dissolution reaction in the rock matrix has caused

916 consumption of CO_{2aq} and reduced its mass along the leakage pathway.

917 This study has quantified the amount of CO_{2aq} uptake in various aqueous phase equilibrium

918 and calcite kinetic reactions along a fractured pathway under a few hypothetical leakage

919 scenarios. In the reactive transport scenarios considered, the transport retardation in

920 CO_{2aq} and its mass uptake in geochemical reactions along the flow pathway was found

921 to be sensitive to various physical and geochemical processes and parameters. The total

922 mass uptake of CO_{2aq} in geochemical reactions increases with increase in fluid velocity

923 in the fracture, diffusion coefficient and sorption partition coefficient, whereas it

924 decreases with increasing temperature along the leakage pathway. After 500 years of

925 simulation for the selected set of parameters in the various reactive transport scenarios, the

926 normalized mass uptake of CO_{2aq} was found to be 4.43% for the no sorption case and up to

927 5.46% for the sorption case.

928

929 The analysis presented here retains a number of limitations that might be addressed by future

930 studies. In particular, the mineralogical composition of clay caprock considered here is very

931 site specific, and only the kinetics of calcite mineral is considered, thereby ignoring the role of

932 other minerals due to their slow kinetics. Other simplifications include: the idealized

933 geometry of the fracture, the assumption of a constant porosity in the fracture, and the

934 assumption of constant boundary conditions. Despite these simplifications, this analysis

935 captures the most salient aspects of CO_{2aq} leakage along the fractured pathway in the clay

936 caprock. The reactive transport model presented here can be applied to study the leakage of

937 CO_2-saturated brine in the fractured rock formation where calcite is the major rock forming

938 mineral. Future studies should further extend this modeling framework by considering the

939 velocity field in the fracture and in the rock matrix coupled with the porosity and permeability

940 variations due to mineral dissolution and precipitation.

941

949

950

951   APPENDICES

952   **Appendix A: Solution procedure for a system of mixed equilibrium and mineral kinetic**

953   **reactions**

954   Here we present the methodology of writing the aqueous chemical species in terms of

955   chemical components, formulation of related algebraic equations required for speciation and

956   deriving the reaction term (r_{kin}) that appears in the reactive transport equation.

957   *A.1.   Equilibrium reactions for batch geochemical modeling*

958   The five equilibrium reactions considered in the batch reaction modeling are displayed as

959   (R0)-(R4) in Table 1. Despite the presence of brine, the dissolution of NaCl in the reactive

960   system does not need to be calculated because we can assume that halite saturation is not

961   reached and precipitation never occurs. Also considering chloride (Cl^{-1}) as a conservative

962   solute it is fully decoupled from the geochemical system. The activity of H_2O was assumed as

963   unity and is not considered in the list of either primary or secondary species (Saaltink et al.,

964   1998). The equilibrium geochemical system involves seven aqueous chemical species (HCO_3^-

965   , Na^+, CO_{2aq}, H^+, OH^-, CO_3^{2-}, and $NaHCO_{3aq}$). These species, N_s^{eq} (= 7) appear in five N_e (=

966   5) independent equilibrium reactions.

967   *A.2.   Equilibrium reactions for reactive transport modeling*

968   In reactive transport modeling, the equilibrium between the gas (CO_{2g}) and dissolved phase

969   (CO_{2aq}) is not considered and is excluded from the list of equilibrium reactions. Here, the

970   geochemical system involves the same seven aqueous chemical species (N_s^{eq} = 7), which

971   now appear in four equilibrium reactions (N_e = 4). In this study, species Ca^{2+} is only involved

972   in the kinetic reaction of mineral calcite and does not participate in any of the equilibrium

973   reactions. Here, we call this species (Ca^{2+}) the only-kinetic species (N_s^{kin} = 1). The species

974   involved in all of the reactions (equilibrium and kinetic) are classified as primary and

975   secondary. The elimination of the equilibrium reaction term in the reactive transport equation

976   presented by Saaltink et al., 1998 requires that the stoichiometric reaction matrices must be of

977   an appropriate size. Saaltink et al., 1998 presented a method for eliminating equilibrium

978   reactions term in the reactions scenarios, in which the species involved in the kinetic reactions

979   also participate in the equilibrium reactions. In this study, to produce correctly sized matrices

980   (explained below), we also included the only-kinetic species in the list of primary species.

981   Thus, the total number of species involved in the equilibrium plus the kinetic reactions

982   becomes eight ($N_s^{tot} = N_s^{eq} + N_s^{kin}$). The equilibrium reactions are described by the law of

983   mass action and can be written in matrix form as follows:

984     $$\mathbf{S_{eq}} \log \mathbf{a} = \log \mathbf{K} \tag{A1}$$

985   where $\mathbf{a}$ is the vector of activities of all the aqueous species, $\mathbf{K}$ is the vector of equilibrium

986   reaction constants, and $\mathbf{S_{eq}}$ is a matrix (size $N_e \times N_s^{tot}$) containing the stoichiometric

987   coefficients of the equilibrium reactions. We have selected HCO_3^-, Na^+, CO_{2aq} and Ca^{2+} as

988   the four primary species ($N_s^p = N_s^{tot} - N_e = 4$). The four remaining species (H^+, OH^-, CO_3^{2-}

989   and, $NaHCO_{3aq}$) are designated as secondary. While the only-kinetic species are included in

990   the list of primary species, the stoichiometry of the resulting reaction matrix ensures that the

991   changes in the concentrations of the only-kinetic species only depend on the kinetic reaction

992   and are not affected by any of the equilibrium reactions. With this choice, the equilibrium

993   reaction matrix $\mathbf{S_{eq}}$ is split into two portions that represent the primary and secondary

994   species as follows:

995     $$\mathbf{S_{eq}} = [\mathbf{S}_1 \quad \mathbf{S}_2] \tag{A2}$$

996   where $\mathbf{S_1}$ is the sub-matrix $(N_e \times N_s^{tot} - N_e)$, and $\mathbf{S_2}$ is the square sub-matrix $(N_e \times N_e)$.

997   From equilibrium reactions (R1) through (R4) (in Table 1), the actual matrices can be written

998   as follows:

999     $$\mathbf{S_1} = \begin{bmatrix} HCO_3^- & Na^+ & CO_{2aq} & Ca^{2+} \\ 1 & 0 & -1 & 0 \\ 0 & 0 & 0 & 0 \\ -1 & 0 & 0 & 0 \\ -1 & -1 & 0 & 0 \end{bmatrix}$$

1000 $$\mathbf{S_2} = \begin{bmatrix} H^+ & OH^- & CO_3^{2-} & NaHCO_{3aq} \\ 1 & 0 & 0 & 0 \\ 1 & 1 & 0 & 0 \\ 1 & 0 & 1 & 0 \\ 0 & 0 & 0 & 1 \end{bmatrix}$$

1001 $$\mathbf{S_{eq}} = \begin{bmatrix} HCO_3^- & Na^+ & CO_{2aq} & Ca^{2+} & H^+ & OH^- & CO_3^{2-} & NaHCO_{3aq} \\ 1 & 0 & -1 & 0 & 1 & 0 & 0 & 0 \\ 0 & 0 & 0 & 0 & 1 & 1 & 0 & 0 \\ -1 & 0 & 0 & 0 & 1 & 0 & 1 & 0 \\ -1 & -1 & 0 & 0 & 0 & 0 & 0 & 1 \end{bmatrix}$$

1002   *A.3.*   *Reducing the order of the reactive transport system*

1003   The reaction term ($\mathbf{r_{kin}}$) in the reactive transport equation can be explicitly written as a linear

1004   combination of all the reactions presented in Table 1 ((R1) through (R5)). The coefficients of

1005   these linear combinations form a stoichiometric matrix. In short, it is possible to write the

1006   following:

1007 $\mathbf{r_{kin}} = \mathbf{S}^\mathbf{T} r$ (A3)

1008   This equation can be split into two parts to separately account for the equilibrium and kinetic

1009   reactions as follows:

1010 $$\mathbf{r_{kin}} = \mathbf{S_{eq}^T} r_{eq} + \mathbf{S_{kin}^T} r_m \qquad (A4)$$

1011 where $\mathbf{S_{eq}^T}$ is a transpose of $\mathbf{S_{eq}}$, r_m represents the mineral kinetic reaction that is defined

1012 in equation (5), and $\mathbf{S_{kin}^T}$ is a transpose of the matrix of all the dissolved species, which

1013 represents their stoichiometry in the mineral kinetic reactions ($\mathbf{S_{kin}}$):

1014 $$\mathbf{S_{kin}^T} = \begin{bmatrix} HCO_3^- & Na^+ & CO_{2aq} & Ca^{2+} & H^+ & OH^- & CO_3^{2-} & NaHCO_{3aq} \\ 1 & 0 & 0 & 1 & -1 & 0 & 0 & 0 \end{bmatrix}$$

1015 For the kinetic reactions, the rate can be computed from the activities of the species.

1016 However, for the equilibrium reactions, the rates are in principle undetermined. Thus, the

1017 equilibrium reaction term is described by equilibrium laws, which are algebraic expressions.

1018 The considered geochemical system involves eight chemical species that are involved in

1019 equilibrium and mineral kinetic reactions and requires eight transport equations. However, the

1020 number of transport equations can be reduced by eliminating the equilibrium reaction term (

1021 $\mathbf{r_{eq}}$) (Saaltink et al., 1998). To eliminate the equilibrium reaction rates in the transport

1022 equation, a kernel matrix ($\mathbf{U}$) can be defined as follows (Saaltink et al., 1998):

1023 $$\mathbf{U S_{eq}^T} = 0 \Rightarrow \mathbf{U S_{eq}^T r_{eq}} = 0 \qquad (A5)$$

1024 The matrix $\mathbf{U}$ is given as

1025 $$\mathbf{U} = \begin{bmatrix} \mathbf{I}_{N_s^{tot} - N_e} & \left(-\mathbf{S_2^{-1} S_1} \right)^{\mathbf{T}} \end{bmatrix} \qquad (A6)$$

1026 where $\mathbf{I}_{N_s^{tot} - N_e}$ denotes the identity matrix with $N_s^{tot} - N_e$ rows and columns. The matrix

1027 $\mathbf{U}$ is referred to as the "component matrix" because it adds up the total amount of a chemical

1028 component distributed over various aqueous chemical species involved in chemical reactions.

1029   The process of defining the component matrix requires that the matrix $\mathbf{S_2}$ must be invertible.

1030   After some algebra, the resulting matrix is written as follows:

1031
$$\mathbf{U} = \begin{pmatrix} \dfrac{\text{species}}{\text{components}} & HCO_3^- & Na^+ & CO_{2aq} & Ca^{2+} & H^+ & OH^- & CO_3^{2-} & NaHCO_{3aq} \\ u_{HCO_3} & 1 & 0 & 0 & 0 & -1 & 1 & 2 & 1 \\ u_{Na} & 0 & 1 & 0 & 0 & 0 & 0 & 0 & 1 \\ u_{CO_2} & 0 & 0 & 1 & 0 & 1 & -1 & -1 & 0 \\ u_{Ca} & 0 & 0 & 0 & 1 & 0 & 0 & 0 & 0 \end{pmatrix}$$

1032   By pre-multiplying the concentration vector ($\mathbf{c}$) of the species involved in all of the reactions

1033   by the component matrix ($\mathbf{U}$), we can obtain the total concentrations of the four chemical

1034   components as a linear combination of the dissolved species as follows:

1035 $\mathbf{u} = \mathbf{Uc}$ (A7)

1036   where $\mathbf{u}$ is the vector of the total concentrations of the components. Equation (A7) results in

1037   the following four chemical components that are involved in the reactive transport equation:

1038
$$\begin{cases} u_{HCO_3} = c_{HCO_3^-} - c_{H^+} + c_{OH^-} + 2c_{CO_3^{2-}} + c_{NaHCO_{3aq}} \\ u_{Na} = c_{Na^+} + c_{NaHCO_{3aq}} \\ u_{CO_2} = c_{CO_{2aq}} + c_{H^+} - c_{OH^-} - c_{CO_3^{2-}} \\ u_{Ca} = c_{Ca^{2+}} \end{cases}$$

1039   for the following components vector ($\mathbf{u}$):

1040
$$\mathbf{u} = \begin{bmatrix} u_{HCO_3} \\ u_{Na} \\ u_{CO_2} \\ u_{Ca} \end{bmatrix}$$

1041   By introducing the component matrix ($\mathbf{U}$), the required number of transport equations has

1042   been reduced to four (equal to the number of chemical components) from eight (equal to the

1043   number of aqueous species). After eliminating the equilibrium reactions term, the reaction

1044   term in equation (A4) is reduced as follows:

1045 $$\mathbf{r_{kin}} = \mathbf{US_{kin}^T} r_m \qquad (A8)$$

1046 The product of first two terms in equation (A8) results in the following vector:

1047 $$\mathbf{US_{kin}^T} = \begin{bmatrix} 2 \\ 0 \\ -1 \\ 1 \end{bmatrix}$$

1048 Thus equation (A8) can be written in the following forms:

1049 $$\mathbf{r_{kin}} = \mathbf{US_{kin}^T} r_{kin}^m = \begin{bmatrix} 2 \\ 0 \\ -1 \\ 1 \end{bmatrix} [r_m] \qquad (A9)$$

1050 $$\mathbf{r_{kin}} = \begin{cases} r_{u_{HCO_3}} = 2r_m \\ r_{u_{Na}} = 0r_m \\ r_{u_{CO_2}} = -r_m \\ r_{u_{Ca}} = r_m \end{cases} \qquad (A10)$$

1051 Thus, the reaction term ($\mathbf{r_{kin}}$) in equation (A10) provides information regarding the

1052 consumption or production of all four chemical components involved (thereby considering the

1053 combined effects of equilibrium and the mineral kinetic reactions) in the reactive transport

1054 equation.

1055 *A.4.   Speciation modeling*

1056 We refer to the process of finding the individual aqueous species concentrations from the

1057 chemical components as speciation modeling. Because the chemical components have been

1058 written as linear combinations of aqueous species, we must solve algebraic equations to

1059 calculate the concentration of aqueous species.

1060 *A.4.1. Batch geochemical modeling*

1061   A system of eight algebraic equations (A11 through A18) results from considered five

1062   equilibrium reactions ((R0) through (R4)) and one kinetic reaction (R5) that must be solved

1063   for eight dissolved species (HCO_3^-, Na^+, CO_{2aq}, Ca^{2+}, H^+, OH^-, CO_3^{2-} and $NaHCO_{3aq}$). One

1064   algebraic equation (A18) emerges from the only-kinetic species (Ca^{2+}). These algebraic

1065   equations are solved in COMSOL until the residual of the equations are lower than a certain

1066   tolerance limit.

1067
$$\left(c_{CO_{2aq}} \gamma_{CO_{2aq}} \right) - \left(K_{CO_{2g}} \right) = 0 \tag{A11}$$

1068
$$\left(c_{H^+} \gamma_{H^+} c_{HCO_3^-} \gamma_{HCO_3^-} \right) - \left(c_{CO_{2aq}} \gamma_{CO_{2aq}} K_{CO_{2aq}} \right) = 0 \tag{A12}$$

1069
$$\left(c_{H^+} \gamma_{H^+} c_{OH^-} \gamma_{OH^-} \right) - \left(K_{H_2O} \right) = 0 \tag{A13}$$

1070
$$\left(c_{H^+} \gamma_{H^+} c_{CO_3^{2-}} \gamma_{CO_3^{2-}} \right) - \left(c_{HCO_3^-} \gamma_{HCO_3^-} K_{HCO_3^-} \right) = 0 \tag{A14}$$

1071
$$\left(c_{NaHCO_{3aq}} \gamma_{NaHCO_{3aq}} \right) - \left(c_{Na^+} \gamma_{Na^+} c_{HCO_3^-} \gamma_{HCO_3^-} K_{Na^+} \right) = 0 \tag{A15}$$

1072
$$u_{HCO_3} - \left(c_{HCO_3^-} - c_{H^+} + c_{OH^-} + 2c_{CO_3^{2-}} + c_{NaHCO_{3aq}} \right) = 0 \tag{A16}$$

1073
$$u_{Na} - \left(c_{Na^+} + c_{NaHCO_{3aq}} \right) = 0 \tag{A17}$$

1074
$$u_{Ca} = c_{Ca^{2+}} \tag{A18}$$

1075   In the equations above, the symbol γ_i represents the activity coefficient of the aqueous

1076   species. The detailed methodology of calculating the activity coefficient of aqueous species is

1077   presented in Appendix B.

1078 *A.4.1.1. Solution of component species*

1079 In the batch geochemical modeling, the component species are defined in terms of ordinary

1080 differential equations (ODEs) as follows:

1081
$$u_{HCO_3} = \frac{d}{dt} u_{HCO_3} - r_{u_{HCO_3}}$$
(A19)

1082
$$u_{Na} = \frac{d}{dt} u_{Na} - r_{u_{Na}}$$
(A20)

1083
$$u_{Ca} = \frac{d}{dt} u_{Ca} - r_{u_{Ca}}$$
(A21)

1084 In the above equations, the symbol r represents the reaction rates of the respective chemical

1085 components which have been defined in equation (A10).

1086 *A.4.2. Reactive transport*

1087 Transport of the chemical components by the reactive transport equation requires the

1088 calculation of the aqueous species at every node of the computational domain for their

1089 participation in the equilibrium and kinetic reactions. The following eight algebraic equations

1090 (A22 through A29) resulted from four equilibrium reactions ((R1) through (R4)) and one

1091 mineral kinetic reaction (R5):

1092
$$\left(c_{H^+} \gamma_{H^+} c_{HCO_3^-} \gamma_{HCO_3^-} \right) - \left(c_{CO_{2aq}} \gamma_{CO_{2aq}} K_{CO_{2aq}} \right) = 0$$
(A22)

1093
$$\left(c_{H^+} \gamma_{H^+} c_{OH^-} \gamma_{OH^-} \right) - \left(K_{H_2O} \right) = 0$$
(A23)

1094
$$\left(c_{H^+} \gamma_{H^+} c_{CO_3^{2-}} \gamma_{CO_3^{2-}} \right) - \left(c_{HCO_3^-} \gamma_{HCO_3^-} K_{HCO_3^-} \right) = 0$$
(A24)

1095
$$\left(c_{NaHCO_{3aq}} \gamma_{NaHCO_{3aq}} \right) - \left(c_{Na^+} \gamma_{Na^+} c_{HCO_3^-} \gamma_{HCO_3^-} K_{Na^+} \right) = 0$$
(A25)

1096
$$u_{HCO_3} - \left(c_{HCO_3^-} - c_{H^+} + c_{OH^-} + 2c_{CO_3^{2-}} + c_{NaHCO_{3aq}} \right) = 0$$
(A26)

53

1097 $$u_{Na} - \left(c_{Na^+} + c_{NaHCO_{3aq}} \right) = 0 \qquad \text{(A27)}$$

1098 $$u_{CO_2} - \left(c_{CO_{2aq}} + c_{H^+} - c_{OH^-} - c_{CO_3^{2-}} \right) = 0 \qquad \text{(A28)}$$

1099 $$u_{Ca} = c_{Ca^{2+}} \qquad \text{(A29)}$$

1100 Because one aqueous species (Ca^{2+}) only participates in the kinetic reaction of mineral calcite,

1101 its concentration is equal to the respective chemical component that is being transported by

1102 the reactive transport equation.

1103 **Appendix B: Activity coefficients of aqueous species**

1104 The activities of aqueous species are related to their concentration (c) through the activity

1105 coefficient (γ) as follows (Lide et al., 2010):

1106 $$a_i = \gamma_i \frac{c_i}{c_0} \qquad \text{(B1)}$$

1107 where c_0 is the standard concentration [1 mol/(kg water)], c_i is the molality [mol/(kg water)]

1108 of the i-th species of the solution and γ_i is the concentration dependent activity coefficient.

1109 The species activity is thus a dimensionless quantity.

1110
1111 The activity coefficients depend on the ionic strength (μ) of the solution defined as follows:

1112 $$\mu = \frac{1}{2} \sum c_i z_i^2 \qquad \text{(B2)}$$

1113 A summation is extended over all charged species (c_i), and z_i represents the charge of

1114 species i.

1115 *B.1.   CO_{2aq}*

1116 A virial expansion based on excess Gibbs free energy from (Pitzer, 1973) is used to calculate

1117 the activity coefficient of CO_{2aq} as follows (Duan & Sun, 2003):

54

1118
$$\ln \gamma_{CO_2} = 2\lambda_{CO_2\text{-}Na}\left(c_{Na^+} + c_{K^+} + 2c_{Ca^{2+}} + 2c_{Mg^{2+}} \right)$$ (B3)

$$-\xi_{CO_2\text{-}Na\text{-}Cl}\left(c_{Cl^-} \right)\left(c_{Na^+} + c_{K^+} + c_{Ca^{2+}} + c_{Mg^{2+}} \right) - 0.07 c_{SO_4^{2-}}$$

1119 *B.2.   Charged species*

1120 The activity coefficients of charged aqueous species for low-ionic strength solutions (up to 3

1121 molal of NaCl dominant solutions) are obtained from the extended Debye-Hückel function

1122 (B-dot model) as follows:

1123 $$\log \gamma_i = -A_\gamma \left(z^2 \right) \sqrt{\overline{I}} \Big/ \left(1 + \dot{a} B_\gamma \sqrt{\overline{I}} \right) + \dot{B}\overline{I}$$ (B4)

1124 *B.3.   Uncharged species*

1125 The activity coefficients of the electrically neutral, non-polar species are calculated from the

1126 following relationship (Betheke, 2008):

1127 $$\log \gamma_j = aI + bI^2 + cI^3$$ (B5)

1128 with the corresponding parameters available in Table B 1. Linear interpolation is used to find

1129 the values of the constants (a , b and c) at the temperature of interest.

1130 **Table B 1.** Parameters for equation (B5).

T [°C]	a	b	c
25	0.1127	-0.01049	1.545×10^{-3}
100	0.08018	-0.001503	0.5009×10^{-3}
200	0.09892	-0.01040	1.386×10^{-3}
300	0.1967	-0.01809	-2.497×10^{-3}

1131

1132 *B.4.   Water*

1133 Although different models are available for evaluating the activity of water, the activity of

1134 water is assumed as constant and equal to unity in this study (Saaltink et al., 1998).

1135 **Appendix C: Viscosity of brine**

1136 According to Mao & Duan, 2009, the viscosity of brine ($NaCl+H_2O$) can be determined from

1137 the following relationship:

1138 $\mu_{sol} = \mu_r \mu_{H_2O}$ (C1)

1139 where μ_{sol} represents the solution viscosity [Pa s], μ_r refers to the relative viscosity, and

1140 μ_{H_2O} is the viscosity of pure water in [Pa s]. The relative viscosity is found from the

1141 following relationship:

1142 $\mu_r = \exp\left(Am + Bm^2 + Cm^3\right)$ (C2)

1143 where m is the molality [mol/(kg water)] of salt (NaCl) and A, B, and C are polynomials

1144 defined as a function of temperature T [K]:

1145 $\begin{cases} A = a_0 + a_1 T + a_2 T^2 \\ B = b_0 + b_1 T + b_2 T^2 \\ C = c_0 + c_1 T \end{cases}$ (C3)

1146 The parameters (a_i, b_i and c_i) are given in Table C 1.

1147 **Table C 1.** Parameters for equation (C3).

i	a_i	b_i	c_i
0	-0.21319213	0.69161945×10^{-1}	-0.2598886×10^{-2}
1	0.1365159×10^{-2}	-0.2729226×10^{-3}	0.7798923×10^{-5}
2	-0.1219176×10^{-5}	0.2085245×10^{-6}	——

1148

1149 The viscosity of pure water was calculated from the following relationship:

1150 $\mu_{H_2O} = \exp\left(\sum_{i=1}^{5} d_i T^{i-3} + \sum_{i=6}^{10} d_i \rho_{H_2O} T^{i-8}\right)$ (C4)

1151 where the density of pure water (ρ_{H_2O}) was found from Cooper & Dooley, 2007 and the

1152 parameters (d_i) are given in Table C 2.

56

1153   **Table C 2.** Parameters for equation (C4).

i	d_i	i	d_i
1	0.28853170×10^7	6	-0.19283851×10^7
2	-0.11072577×10^5	7	0.56216064×10^4
3	-0.90834095×10^1	8	0.13827250×10^2
4	$0.30925651 \times 10^{-1}$	9	$-0.47609523 \times 10^{-1}$
5	$-0.27407100 \times 10^{-4}$	10	$0.35545041 \times 10^{-4}$

1154

1155

1156

1157 **References**

1158 Al-Rawajfeh, A.E., 2004. Modeling and simulation of CO_2 release in multiple-effect distillers

1159   for seawater desalination, Ph.D. Dissertation. Department of Engineering Sciences,

1160   Institute of Thermal Process Engineering, Martin-Luther University of Halle-

1161   Wittenberg, Halle(Saale), Germany.

1162 Andreani, M., Gouze, P., Luquot, L., Jouanna, P., 2008. Changes in seal capacity of fractured

1163   claystone caprocks induced by dissolved and gaseous CO_2 seepage. Geophys. Res. Lett.

1164   35, L14404. doi:10.1029/2008GL034467.

1165 Arts, R., Chadwick A., Eiken, O., 2005. Recent time-lapse seismic data show no indication of

1166   leakage at the Sleipner CO_2-injection site. Greenhouse Gas Control Technologies,

1167   Volume 1.

1168 Audigane, P., Gaus, I., Pruess, K., Xu, T., 2005. Reactive transport modeling using

1169   TOUGHREACTE for the long term CO_2 storage at Sleipner, Nort Sea. Conference

1170   Proceedings, 4th Annual conference on carbon capture and sequestration DOE/NETL,

1171   May 2-5, 2005.

1172 Audigane, P., Gaus, I., Czernichowski-Lauriol, I., Pruess, K., Xu, T., 2007. Two-dimensional

1173   reactive transport modeling of CO_2 injection in a saline aquifer at the Sleipner site,

1174   North Sea. Am. J. Sci. 307 (7), 974-1008. doi:10.2475/07.2007.02.

1175 Bachu, S., Gunter, W.D., and Perkins, E.H., 1994. Aquifer disposal of CO_2: hydrodynamic

1176   and mineral trapping. Energ. Convers. Manage. 35(4), 269-279.

1177 Bear, J., Cheng, A.H..-D., 2010. Modeling groundwater flow and contaminant transport. Vol.

1178   23, ISBN, 978-1-4020-6681-8, Springer, Dordrecht. doi:10.1007/978-1-4020-6682-5.

1179 Betheke, C.M., 2008. Geochemical and Biogeochemical Reaction Modeling, second

1180   ed., ISBN-13 978-0-511-37897-3. Cambridge University Press, New York.

1181 Bodin, J., Delay, F., de Marsily, G., 2003. Solute transport in a single fracture with negligible

1182   matrix permeability: 2. Mathematical formalism. Hydrogeol. J 11 (4), 434-454.

1183   doi:10.1007/s10040-003-0269-1.

1184 COMSOL. The Platform for Physics-Based Modeling and Simulation. COMSOL AB,

1185   Stockholm, Sweden.

1186 Cooper, J.R., and Dooley, R.B., 2007. IAPWS-IF97, Revised release on the IAPWS Industrial

1187   Formulation 1997 for the Thermodynamic Properties of Water and Steam (The revision

1188   only relates to the extension of region 5 to 50 MPa). The International Association for

1189   the Properties of Water and Steam.

1190 Cvetkovic, V., Selroos, J.O., Cheng, H., 1999. Transport of reactive tracers in rock

1191   fractures. J. Fluid Mech. 378, 335-356. doi:10.1017/S0022112098003450.

1192 Dreybrodt, W., Lauckner, J., Zaihua, L., Svensson, U., and Buhmann, D., 1996. The kinetics

1193   of the reaction in the $CO_2+H_2O \rightarrow H^++HCO_3^-$ as one of the rate limiting steps for the

1194   dissolution of calcite in the system H_2O-CO_2-$CaCO_3$, Geochemica et Cosmochimica

1195   Acta, 60(18), 3375-3381.

1196 Dreybrodt, W., Eisenlohr, L., Madry, B., and Ringer, S., 1997. Precipitation kinetics of calcite

1197   in the system $CaCO_3$-H_2O-CO_2: The conversion to CO_2 by the slow process $H^++HCO_3^-$

1198 $\rightarrow CO_2+H_2O$ as a rate limiting step, Geochemica et Cosmochimica Acta, 61(18), 3897-

1199   3904.

1200 Duan, Z., Sun, R., 2003. An improved model calculating CO_2 solubility in pure water and

1201   aqueous NaCl solutions from 273 to 533 K and from 0 to 2000 bar. Chem. Geol. 193 (3-

1202   4), 257-271. doi:10.1016/S0009-2541(02)00263-2.

1203 Duan, Z., Sun, R., Zhu, C., Chou, I., 2006. An improved model for the calculation of CO_2

1204   solubility in aqueous solutions containing Na^+, K^+, Ca^{2+}, Mg^{2+}, Cl^-, and SO_4^{2-}. Mar.

1205   Chem. 98 (2-4), 131-139. doi:10.1016/j.marchem.2005.09.001.

1206 Ellis, B.R., Bromhal, G.S., McIntyre, D.L., Peters, C.A., 2011. Changes in caprock integrity

1207   due to vertical migration of CO_2-enriched brine. Energ. Procedia 4, 5327-5334.

1208 Fujii, T., Nakagawa, S., Sato, Y., Inomata, H., Hashida, T., 2010. Sorption characteristics of

1209 CO_2 on rocks and minerals in storing CO_2 processes. Natural Res. 1 (1), 1-10.

1210 Gaus, I., 2010. Role and impact of CO_2-rock interactions during CO_2 storage in sedimentary

1211   rocks. Int. J. Greenh. Gas Con. 4 (1), 73-89. doi:10.1016/j.ijggc.2009.09.015.

1212 Gherardi, F., Xu, T., Pruess, K., 2007. Numerical modeling of self-limiting and self-

1213   enhancing caprock alteration induced by CO_2 storage in a depleted gas reservoir. Chem.

1214   Geol. 244 (1-2), 103-129. doi:10.1016/j.chemgeo.2007.06.009.

1215 Grisak, G.E., Pickens, J.F., 1980. Solute transport through fractured media 1. The effect of

1216   matrix diffusion. Water Resour. Res. 16 (4), 719-730.

1217 Gunter, W.D., Perkins, E.H., and McCANN, T.J., 1993. Aquifer disposal of CO_2-rich gases:

1218   reaction design for added capacity. Energy Convers. Mgmt Vol. 34(9-11), 941-948.

1219 Hassanzadeh,   H.,   Pooladi-

1220   Darvish, M., Elsharkawy, A.M., Keith, D.W., Leonenko, Y., 2008. Predicting PVT data

1221   for CO_2-brine mixtures for black-oil simulation of CO_2 geological storage. Int. J.

1222   Greenh. Gas Con. 2, 65-77.

1223 Haugan, P.M., Joos, F., 2004. Metrics to assess the mitigation of global warming by carbon

1224   capture and storage in the ocean and in geological reservoirs. Geophys. Res. Lett.

1225   31, L18202.

1226 Heller, R., and Zoback, M., 2014. Adsorption of methane and carbon dioxide on gas shale and

1227   pure mineral samples. Unconventional Oil Gas Resour. 8, 14-24.

1228 Hellevang, H., 2006. Interactions between CO_2, Saline Water and Minerals during Geological

1229   Storage of CO_2, Ph.D. Thesis. University of Bergen, Norway.

1230   Holloway, S., 1997. An overview of the underground disposal of carbon dioxide. Energ.

1231   Convers. Manage. 38, S193-S198. doi:10.1016/S0196-8904(96)00268-3.

1232   Holloway, S., 2005. Underground sequestration of carbon dioxide-a viable greenhouse gas

1233   mitigation option. Energy 30 (11-12), 2318-2333. doi:10.1016/j.energy.2003.10.023.

1234   Intergovernmental Panel of Climate Change, 2002. IPCC Workshop on Carbon Dioxide

1235   Capture and Storage, Proceedings. Regina, Canada.

1236   Intergovernmental Panel of Climate Change, 2005. IPCC Special Report on Carbon Dioxide

1237   Capture and Storage. Cambridge University Press, New York, America.

1238   Johnson, J.W., Nitao, J.J., and Knauss K.G., 2004. Reactive transport modelling of CO_2

1239   storage in saline aquifers to elucidate fundamental processes, trapping mechanisms,

1240   and sequestration partitioning. Geological Society of London Special Publication on

1241   Carbon Sequestration Technologies.

1242   Kaufmann, G., Dreybrodt, W., 2007. Calcite dissolution kinetics in the system $CaCO_3$-H_2O-

1243 CO_2 at high undersaturation. Geochim. Cosmochim. Acta 71 (6), 1398-1410.

1244   doi:10.1016/j.gca.2006.10.024.

1245   Lai, K-H., Chen, J-S., Liu, C-W., and Yang, S-Y., 2014. Effect of permeability-porosity

1246   functions on simulated morphological evolution of a chemical dissolution front. Hydrol.

1247   Process. 28, 16-24. doi: 10.1002/hyp.9492.

1248   Langmuir D, 1997. Aqueous Environmental Geochemistry. ISBN 0-02-367412-1, Prentice

1249   Hall, New Jersey.

1250   Lasaga, A.C., 1984. Chemical kinetics of water-rock interaction. J. Geophys. Res. 89

1251   (B6), 4009-4025.

1252   Lasaga, A.C., Soler, J.M., Ganor, J., Bruch, T.E., Nagy, K.L., 1994. Chemical weathering rate

1253   laws and global geochemical cycles. Geochim. Cosmochim. Acta 58 (10), 2361-2386.

1254 Lide D.R., ed., 2010. CRC Handbook of Chemistry and Physics. 90th Edition (CD-ROM
1255   Version 2010), CRC Press/Taylor and Francis, Boca Raton,
1256   FL.Mao, S., Duan, Z., 2009. The viscosity of aqueous alkali-chloride solutions up to
1257   623K, 1000 bar, and high ionic strength. Int. J. Thermophys. 30 (5), 1510-1523.
1258   doi:10.1007/s10765-009-0646-7.

1259 Mao S., and Duan Z. (2009), The viscosity of aqueous alkali-chloride solutions up to 623K,
1260   1000 bar, and high ionic strength, Int. J. Thermophys., 30, 1510-1523.

1261 Marini, L., 2007. Sequestration of carbon dioxide; thermodynamics kinetics and reaction path
1262   modeling. ISBN-13:978-0-444-52950-3. Elsevier, Netherlands and UK.

1263 Middleton, R.S., Keating, G.N., Stauffer, P.H., Jordan, A.B., Viswanathan, H.S., Kang, Q.J.,
1264   2012. The cross-scale science of CO2 capture and storage: from pore scale to regional
1265   scale. Energ. Environ. Sci. 5 (6), 7328-7345. doi:10.1039/c2ee03227a.

1266 Neretnieks, I., 1980. Diffusion in the rock matrix: an important factor in radionuclide
1267   retardation? J. Geophys. Res. 85 (B8), 4379-4397. doi:10.1029/JB085iB08p04379.

1268 Nogues, J.P., Fitts, J.P., Celia, M.A., Peters, C.A., 2013. Permeability evolution due to
1269   dissolution and precipitation of carbonates using reactive transport modeling in pore
1270   networks. Water Resour. Res. 49, 6006-6021. doi:10.1002/wrcr.20486.

1271 Novak, C.F., 1993. Modeling mineral dissolution and precipitation in dual-porosity fracture-
1272   matrix system. J. Cont. Hydrol. 13, 91-115.

1273 Novak, C.F., 1996. Development of the FMT chemical transport simulator: coupling aqueous
1274   density and mineral volume fraction to phase compositions. J. Cont. Hydrol. 21 (1-
1275   4), 297-310. doi:10.1016/0169-7722(95)00055-0.

1276 Orr, Jr., F.M., 2009. CO_2 capture and storage: are we ready? Energ. Environ. Sci. 2 (5), 449-
1277   458. doi:10.1039/b822107n.

1278 Peters, C.A., Fitts, J.P., Wilson, E.J., Pollak, M.F., Bielicki, J.M., and Bhatt, V., 2014. Basin-
1279   scale leakage risks from geologic carbon sequestration: impact on carbon capture and
1280   storage energy market competitiveness. Final Scientific/Technical Report,
1281   DOE/FE0000749-41, Princeton University, Princeton, NJ, United States.

1282 Pitzer, S.K., 1973. Thermodynamics of electrolytes. I. Theoretical basis and General
1283   equations. J. Phys. Chem. 77 (2), 268-277.

1284 Pokrovsky, O.S., Golubev, S.V., Schott, J., Castillo, A., 2009. Calcite, dolomite and
1285   magnesite dissolution kinetics in aqueous solutions at acid to circumneutral pH, 25 to
1286   150 °C and 1 to 55 atm pCO_2: new constraints on CO_2 sequestration in sedimentary
1287   basins. Chem. Geol. 265, 20-32.

1288 Pruess, K., 2005. Numerical studies of fluid leakage from a geologic disposal reservoir for
1289 CO_2 show self-limiting feedback between fluid flow and heat transfer. Geophys. Res.
1290   Letters. Vol. 32, L14404, doi: 10.1029/2005GL023250.

1291 Pruess, K., 2006(a). Numerical modeling of CO_2 sequestration in geologic formations-recent
1292   results and open challenges. Earth Sciences Division, Lawrence Berkeley National
1293   Laboratory, University of Californai, Berkeley, CA 94720, USA.

1294 Pruess, K., 2006(b). On leakage from geologic storage reservoirs of CO_2. LBNL-59732.
1295   Lawrence Berkeley National Laboratory.

1296 Pruess, K., 2008. Leakage of CO_2 from geologic storage: Role of secondary accumulation at
1297   shallow depth. Int. J. Greenh. Gas Con. 2, 37-46.

1298 Saaltink, M.W., Ayora, C., Carrera, J., 1998. A mathematical formulation for reactive
1299   transport that eliminates mineral concentrations. Water Resour. Res. 34(7), 1649-1656.

1300 Santschi, C.h, Rossi, M.J., 2006. Uptake of CO_2, SO_2, HNO_3 and HCl on calcite ($CaCO_3$) at
1301   300 K: mechanism and the role of adsorbed water. J. Phys. Chem. A 110 (21), 6789-
1302   6802. doi:10.1021/jp056312b.

1303 Steefel, C.I., Lasaga, A.C., 1994. A coupled model for transport of multiple chemical species

1304   and kinetic precipitation/dissolution reactions with application to reactive flow in single

1305   phase hydrothermal systems. Am.. J. Sci. 294 (5), 529-592. doi:10.2475/ajs.294.5.529.

1306 Steefel, C.I., Lichtner, P.C., 1998(a). Multicomponent reactive transport in discrete fractures

1307   I. Controls on reaction front geometry. J. Hydro. 209, 186-199.

1308 Steefel, C.I., Lichtner, P.C., 1998(b). Multicomponent reactive transport in discrete fractures

1309   II. Infiltration of hyperalkaline groundwater at Maqarin, Jordan, a natural analogue

1310   site. J. Hydro. 209, 200-224.

1311 Stone, E.J., Lowe, J.A., Shine, K.P., 2009. The impact of carbon capture and storage on

1312   climate. Energ. Environ. Sci. 2 (1), 81-91. doi:10.1039/b807747a.

1313 Svensson, U., Dreybrodt, W., 1992. Dissolution kinetics of natural calcite minerals in CO_2-

1314   water systems approaching calcite equilibrium. Chem. Geol. 100, 129-145.

1315 Tabrizy, V.A., Hamouda, A.A., Soubeyrand-Lenoir, E., Denoyel, R., 2013. CO_2 adsorption

1316   isotherm on modified calcite, quartz, and kaolinite surfaces: surface energy analysis.

1317   Pet. Sci. Tech. 31 (15), 1532-1543.

1318 The GEOCHEMIST'S WORKBENCH. An integrated geochemical modeling package.

1319   Aqueous Solutions LLC, Champaign, IL 61820 USA.

1320 Xu, S., Wörman, A., Dverstorp, B., 2001. Heterogeneous matrix diffusion in crystalline rock--

1321   implications for geosphere retardation of migrating radionuclides. J. Contam. Hydrol.

1322   47 (2-4), 365-378.

1323 Xu, T., Sonnenthal, E., Spycher, N., and Zheng, L., 2014. TOUGHREACT V3.0-OMP

1324   Reference Manual: A parallel simulation program for non-isothermal multiphase

1325   geochemical reactive transport. LBNL-DRAFT, Earth Sciences Division, Lawrance

1326   Berkeley National Laboratory, University of California, Berkeley, CA 94720.

1327 Yeh, G-T., and Tripathi, V.S., 1991. A model for simulating transport of reactive multispecies

1328   components: model development and demonstration. Water Resour. Res. 27(12), 3075-

1329   3094.

1330

1331 **Figure captions**

1332 **Figure 1**. Schematic of the transport domain (clayey caprock containing a vertical fracture)
1333 lying above the CO_2 geological storage reservoir.
1334 **Figure 2**. Saturation state of calcite at onset (1 s) of the simulation for (a); scenario-4 (without
1335 sorption); and (b) scenario-5 (with sorption).
1336 **Figure 3**. Calcite reaction rate [mol/(s kg water)] at onset (1 s) of the simulation for; (a)
1337 scenario-4 (without sorption); and (b) scenario-5 (with sorption).
1338 **Figure 4**. Spatial distribution of the concentrations [mol/(kg water)] of dissolved species after
1339 500 years for scenario-5; (a) CO_{2aq}; (b) Ca^{2+}; and (c) HCO_3^{-1}.
1340 **Figure 5**. Effects of the calcite reaction on the; (a) mass of calcite [mol/(m^3 bulk volume)] for
1341 scenario-5; (b) calcite reactive surface area [m^2/(kg water)] for scenario-5 after 500 years.
1342 **Figure 6.** Effects of the calcite reaction on (a) medium porosity for scenario-5; (b) medium
1343 permeability [m^2] for scenario-5; (c) effective diffusivity [m^2/s] for scenario-5 after 500 years.
1344 **Figure 7**. Evolution of pH in the fracture-matrix system after 500 years for various base-case
1345 transport scenarios; (a) scenario-2 (no calcite reaction, no sorption); (b) scenario-3 (no calcite
1346 reaction with sorption); (c) scenario-4 (calcite reaction, no sorption); and (d) scenario-5
1347 (calcite reaction with sorption).
1348 **Figure 8.** The percent normalized uptake of CO_{2aq} in aqueous phase and calcite kinetic
1349 reactions without sorption (scenario-4) and with sorption (scenario-5).
1350 **Figure 9**. Breakthrough curve for the base-case transport scenario-1 showing the
1351 concentration of CO_{2aq} at top outflow of the fracture over the period of time.
1352 **Figure 10**. Breakthrough curves showing the concentration of CO_{2aq} for various base-case
1353 transport scenarios along the fracture, at; (a) 10 m from the inflow boundary; and (b) 20 m
1354 from the inflow boundary.
1355 **Figure 11**. The percent normalized uptake of CO_{2aq} in aqueous phase and calcite kinetic
1356 reactions for various reactive transport scenarios (5.1, 5.2, 5.3, and 5.4) studied in the
1357 sensitivity analysis.
1358 **Figure 12**. The percent normalized mass uptake of CO_{2aq} in aqueous phase and calcite kinetic
1359 reactions for pressure and temperature conditions of: (i) 105 bar and 45°C (scenario-5); and
1360 (ii) 155 bar and 60°C (scenario-5a).

1361

1362

Table 1. Chemical reactions considered for $CaCO_3$-H_2O-CO_2 system.

No.	Reactions and equilibrium reaction constants
(R0)[1]	$CO_{2g} \leftrightarrow CO_{2aq}$
(R1)[2]	$H_2O + CO_{2aq} \leftrightarrow H^+ + HCO_3^-$
(R2)[2]	$H_2O \leftrightarrow H^+ + OH^-$
(R3)[2]	$HCO_3^- \leftrightarrow H^+ + CO_3^{2-}$
(R4)[2]	$Na^+ + HCO_3^- \leftrightarrow NaHCO_{3aq}$
(R5)[2]	$CaCO_3 + H^+ \leftrightarrow Ca^{2+} + HCO_3^-$

1. Equilibrium reaction constant is based on Duan & Sun, 2003 as modified by Duan et

al., 2006; 2. Equilibrium reaction constants are taken from The Geochemist's

Workbench (GWB) (default thermodynamic data for the GWB).

Table 2. Clay caprock mineralogical composition (Gherardi et al., 2007).

Minerals	Volume fraction in solid rock	Volume fraction in porous rock (12% porosity)
Calcite	0.29	0.255
Dolomite	0.04	0.035
Quartz	0.20	0.176
Illite	0.02	0.018
K-feldspar	0	0
Chlorite	0.06	0.053
Albite	0	0
Kaolinite	0.05	0.044
Na-smectite	0.15	0.132
Muscovite	0.19	0.1672

Table 3. Parameters and initial values of variables used in equations (4)-(6) for mineral calcite.

k_{25}* [mol/(s m^2)]	E_a* [KJ/mol]	A_m** [m^2/(kg water)]	$c_{m,bulk}$** [mol/(m^3 bulk volume)]
1.60×10-9	41.87	38.68	6912.5

* From Svensson & Dreybrodt, 1992; **Initial values are calculated from initial volume fraction (corresponding to initial caprock porosity of 0.12) of minerals in porous rock matrix. The minerals reactive surface area is taken equal to 10% of the calculated physical surface area of the respective minerals.

Table 4. Calculated values of viscosities and molecular diffusion coefficients at various pressure and temperature conditions.

Pressure and Temperature	μ_0 [Pa s]	μ_b [Pa s]	D_0 [m^2/s]	D_b [m^2/s]
105 bar and 45℃	5.96×10^{-4}	6.27×10^{-4}	3.19×10^{-9}	3.05×10^{-9}
155 bar and 60℃	4.69×10^{-4}	4.94×10^{-4}	4.25×10^{-9}	4.05×10^{-9}

1381
Table 5. Values of sorption partition coefficient K_d [m^3/kg] deduced from Heller & Zoback, 2014.

Clay sample	Barnett 31	Marcellus	Montney	Eagle Ford 127
Calcite content (%)	0	1	8.1	80
Clay content (%)	37.4	52	24.1	5
K_d [m^3/kg] value at 10.5 MPa	3.18×10^{-3}	1.54×10^{-3}	3.33×10^{-3}	7.39×10^{-4}
K_d [m^3/kg] value at 15.5 MPa	3.45×10^{-3}	1.62×10^{-3}	3.60×10^{-3}	7.93×10^{-4}

1384
1385 **Table 6.** Initial (sub-index 0) and boundary conditions (sub-index bc).

Pressure and temperature	45°C and 105 bar	60°C and 155 bar
Component species	Concentration [mol/(kg water)]	Concentration [mol/(kg water)]
$u_{HCO_3,0}$	4.02×10^{-3}	3.10×10^{-3}
u_{Na_0}	5.00×10^{-1}	5.00×10^{-1}
u_{Ca_0}	2.01×10^{-3}	1.55×10^{-3}
$u_{CO_2,0}$	1.82×10^{-4}	1.38×10^{-4}
$u_{HCO_3,bc}$	7.17×10^{-2}	5.95×10^{-2}
$u_{Na_{bc}}$	5.00×10^{-1}	5.00×10^{-1}
$u_{Ca_{bc}}$	3.58×10^{-2}	2.97×10^{-2}
$u_{CO_2,bc}$	1.08	1.06

1386
1387 **Table 7.** Various base-case transport scenarios.

Scenarios	Processes accounted for
1	No interaction between fracture and matrix
2	Molecular diffusion between fracture and matrix, no calcite mineral reaction in the matrix, no sorption in the matrix
3	Molecular diffusion between fracture and matrix, no calcite mineral reaction in the matrix, sorption in the matrix
4	Molecular diffusion between fracture and matrix, calcite mineral reaction in the matrix, no sorption in the matrix
5	Molecular diffusion between fracture and matrix, calcite mineral reaction in the matrix, sorption in the matrix

1388
1389 **Table 8.** Sensitivity analysis for various parameters using the base-case transport scenarios 3
1390 and 5.

Sub-scenarios	Velocity in the fracture, v [m/s]	Distribution coefficient, K_d [m^3/kg]	Pressure and temperature

3.1	3.17×10^{-8}	2.50×10^{-4}	105 bar and 45°C
3.2	6.34×10^{-7}	2.50×10^{-4}	105 bar and 45°C
3.3	3.17×10^{-7}	7.50×10^{-4}	105 bar and 45°C
3.4	3.17×10^{-7}	8.33×10^{-5}	105 bar and 45°C
5.1	3.17×10^{-8}	2.50×10^{-4}	105 bar and 45°C
5.2	6.34×10^{-7}	2.50×10^{-4}	105 bar and 45°C
5.3	3.17×10^{-7}	7.50×10^{-4}	105 bar and 45°C
5.4	3.17×10^{-7}	8.33×10^{-5}	105 bar and 45°C
3a	3.17×10^{-7}	2.50×10^{-4}	155 bar and 60°C
5a	3.17×10^{-7}	2.50×10^{-4}	155 bar and 60°C

Table 9. Species concentrations from the background BGM at 45°C and 0.01 bar (column 2) and from CO_{2g} dissolution reaction modeling performed at 45°C and 105 bar (column 3).

Pressure and temperature	45°C and 0.01 bar	45°C and 105 bar
Species	c [mol/(kg water)]	c [mol/(kg water)]
HCO_3^-	3.33×10^{-3}	6.04×10^{-2}
Na^+	4.99×10^{-1}	4.89×10^{-1}
Cl^-	5.00×10^{-1}	5.00×10^{-1}
Ca^{2+}	2.01×10^{-3}	3.58×10^{-2}
CO_{2aq}	1.98×10^{-4}	1.08
H^+	5.44×10^{-8}	1.67×10^{-5}
OH^-	1.29×10^{-6}	4.25×10^{-9}
CO_3^{2-}	1.43×10^{-5}	8.85×10^{-7}
$NaHCO_{3aq}$	6.63×10^{-4}	1.13×10^{-2}

Table 10. Mass balance [mol] of CO_{2aq} in the base-case reactive transport scenarios 4 and 5.

Scenarios	Scenario-4	Scenario-5
Total mass entered the domain	1.41×10^4	2.91×10^4
Mass entered the domain due to advection	5.39×10^3	5.39×10^3
Mass entered the domain due to diffusion	8.73×10^3	2.37×10^4
Mass entered the domain due to dispersion	9.15×10^{-5}	2.96×10^{-4}
Mass left the domain	4.27×10^2	9.63×10^{-1}
Mass stored in aqueous state	1.31×10^4	4.68×10^3
Mass stored in adsorbed state	0	2.30×10^4
Mass consumed in geochemical reaction	6.26×10^2	1.45×10^3
% normalized mass uptake of CO_{2aq} after 500 years	4.43	4.98
% error in mass balance	5.44×10^{-2}	6.37×10^{-2}

Table 11. Mass [mol] of CO_{2aq} that entered the domain through bottom inflow boundaries of fracture and rock matrix in the reactive transport scenarios 4 and 5.

Scenarios	Scenario-4		Scenario-5	
Bottom inflow boundary	fracture	matrix	fracture	matrix
Total mass entered the domain	5.39×10^3	8.73×10^3	5.39×10^3	2.37×10^4
Mass entered the domain due to advection	5.39×10^3	0	5.39×10^3	0

Mass entered the domain due to diffusion	4.46×10^{-1}	8.73×10^{3}	1.44×10^{0}	2.37×10^{4}
Mass entered the domain due to dispersion	9.15×10^{-5}	0	2.96×10^{-4}	0

1400

1401 **Table 12**. Mass balance [mol] of Ca^{2+}, mineral calcite and total pore volume of rock matrix in
1402 the base-case reactive transport scenarios 4 and 5 after 500 years.

Scenarios	Scenario-4	Scenario-5
Mass [mol] of Ca^{2+} produced in dissolution of mineral calcite	6.22×10^{2}	1.41×10^{3}
Mass [mol] of mineral calcite dissolved	6.25×10^{2}	1.41×10^{3}
Increase in pore volume [m^{3}]	2.31×10^{-2}	5.21×10^{-2}
% error in mass balance	4.89×10^{-1}	2.35×10^{-1}

1403
1404
1405 **Table 13**. Mass balance [mol] of CO_{2aq} in various reactive transport scenarios (5.1, 5.2, 5.3,
1406 5.4, and 5a) studied in the sensitivity analysis.

Scenarios	Scenario-5.1	Scenario-5.2	Scenario-5.3	Scenario-5.4	Scenario-5a
Total mass entered the domain	2.59×10^{4}	3.37×10^{4}	4.53×10^{4}	2.06×10^{4}	3.21×10^{4}
Mass entered the domain due to advection	5.39×10^{2}	1.08×10^{4}	5.39×10^{3}	5.39×10^{3}	5.29×10^{3}
Mass entered the domain due to diffusion	2.53×10^{4}	2.29×10^{4}	3.99×10^{4}	1.53×10^{4}	2.68×10^{4}
Mass entered the domain due to dispersion	2.96×10^{-5}	2.52×10^{-4}	5.87×10^{-4}	1.71×10^{-4}	3.04×10^{-4}
Mass left the domain	9.11×10^{-2}	2.75×10^{1}	9.11×10^{-1}	1.85×10^{1}	8.12×10^{-1}
Mass stored in aqueous state	4.13×10^{3}	5.42×10^{3}	2.77×10^{3}	7.41×10^{3}	5.18×10^{3}
Mass stored in adsorbed state	2.03×10^{4}	2.66×10^{4}	4.03×10^{4}	1.22×10^{4}	2.55×10^{4}
Mass converted in geochemical reaction	1.44×10^{3}	1.60×10^{3}	2.23×10^{3}	1.03×10^{3}	1.46×10^{3}
% normalized mass uptake of CO_2 after 500 years	5.58	4.75	4.92	5.00	4.55
% error in mass balance	-3.42×10^{-2}	6.03×10^{-2}	6.40×10^{-2}	6.01×10^{-1}	5.90×10^{-2}

1407
1408
1409 **Table 14.** Mass balance [mol] of Ca^{2+}, mineral calcite and pore volume of rock matrix in the
1410 sensitivity analysis (scenarios 5.1, 5.2, 5.3, 5.4, and 5a).

Scenarios	Scenario-5.1	Scenario-5.2	Scenario-5.3	Scenario-5.4	Scenario-5a
Mass [mol] of Ca^{2+} produced in dissolution of mineral calcite	1.37×10^{3}	1.56×10^{3}	2.13×10^{3}	1.01×10^{3}	1.37×10^{3}
Mass [mol] of mineral	1.37×10^{3}	1.57×10^{3}	2.14×10^{3}	1.02×10^{3}	1.38×10^{3}

calcite dissolved					
Increase in pore volume [m^3]	5.07×10^{-2}	5.79×10^{-2}	7.90×10^{-2}	3.75×10^{-2}	5.10×10^{-2}
% error in mass balance	2.46×10^{-1}	2.11×10^{-1}	2.42×10^{-1}	3.02×10^{-1}	3.60×10^{-1}

1411

1412

1413

1414